The Cryosphere Discuss., 8, 2043–2118, 2014
www.the-cryosphere-discuss.net/8/2043/2014/
doi:10.5194/tcd-8-2043-2014
© Author(s) 2014. CC Attribution 3.0 License.

The Cryosphere Discussions
Open Access

This discussion paper is/has been under review for the journal The Cryosphere (TC).
Please refer to the corresponding final paper in TC if available.

Quantifying the Jakobshavn Effect: Jakobshavn Isbrae, Greenland, compared to Byrd Glacier, Antarctica

T. Hughes[1], A. Sargent[2], J. Fastook[3], K. Purdon[4], J. Li[5], J.-B. Yan[5], and S. Gogineni[6]

[1]School of Earth and Climate Sciences, Climate Change Institute, University of Maine, Orono, USA
[2]Department of Mathematics and Statistics, University of Maine, Orono, USA
[3]Computer Sciences Department, Climate Change Institute, University of Maine, Orono, USA
[4]Center for Remote Sensing of Ice Sheets, Geography Department, University of Kansas, Lawrence, USA
[5]Center for Remote Sensing of Ice Sheets, University of Kansas, Lawrence, USA
[6]Center for Remote Sensing of Ice Sheets, Department of Electrical Engineering and Computer Science, University of Kansas, Lawrence, USA

Received: 13 February 2014 – Accepted: 3 April 2014 – Published: 25 April 2014

Correspondence to: T. Hughes (terry.hughes@maine.edu)

Published by Copernicus Publications on behalf of the European Geosciences Union.

Abstract

The Jakobshavn Effect is a series of positive feedback mechanisms that was first observed on Jakobshavn Isbrae, which drains the west-central part of the Greenland Ice Sheet and enters Jakobshavn Isfjord at $69^{\circ}10'$. These mechanisms fall into two categories, reductions of ice-bed coupling beneath an ice stream due to surface meltwater reaching the bed, and reductions in ice-shelf buttressing beyond an ice stream due to disintegration of a laterally confined and locally pinned ice shelf. These uncoupling and unbuttressing mechanisms have recently taken place for Byrd Glacier in Antarctica and Jakobshavn Isbrae in Greenland, respectively. For Byrd Glacier, no surface meltwater reaches the bed. That water is supplied by drainage of two large subglacial lakes where East Antarctic ice converges strongly on Byrd Glacier. Results from modeling both mechanisms are presented here. We find that the Jakobshavn Effect is not active for Byrd Glacier, but is active for Jakobshavn Isbrae, at least for now. Our treatment is holistic in the sense it provides continuity from sheet flow to stream flow to shelf flow. It relies primarily on a force balance, so our results cannot be used to predict long-term behavior of these ice streams. The treatment uses geometrical representations of gravitational and resisting forces that provide a visual understanding of these forces, without involving partial differential equations and continuum mechanics. The Jakobshavn Effect was proposed to facilitate terminations of glaciation cycles during the Quaternary Ice Age by collapsing marine parts of ice sheets. This is unlikely for the Antarctic and Greenland ice sheets, based on our results for Byrd Glacier and Jakobshavn Isbrae, without drastic climate warming in high polar latitudes. Warming would affect other Antarctic ice streams already weakly buttressed or unbuttressed by an ice shelf. Ross Ice Shelf would still protect Byrd Glacier.

TCD
8, 2043–2118, 2014

1 Introduction

The Jakobshavn Effect was fist observed on Jakobshavn Isbrae, an outlet glacier of the Greenland Ice Sheet (Hughes, 1986). It was described as follows: “The Jakobshavn Effect may have been a significant factor in hastening the collapse of paleo ice sheets with the advent of climatic warming after 18 000 years ago and may precipitate partial collapse of the present-day Greenland and Antarctic Ice Sheets following CO_2-induced climate warming in the decades ahead. The Jakobshavn Effect is observed today on Jakobshavn Glacier, which is located at 69°10′ on the west coast of Greenland. The Jakobshavn Effect is a group of positive feedback mechanisms which allow Jakobshavn Glacier to literally pull ice out of the Greenland Ice Sheet at a rate exceeding $7\,\mathrm{km\,a^{-1}}$ across a floating terminus 800 m thick and 6 km wide. The pulling power results from an imbalance of horizontal hydrostatic forces in ice and water columns at the grounding line of the floating terminus. Positive feedback mechanisms that sustain the rapid ice discharge rate are ubiquitous surface crevassing, high summer rates of surface melting, extending creep flow, progressive basal uncoupling, progressive lateral uncoupling, and rapid iceberg calving.”

Surface crevasses multiply the area exposed to solar radiation, with multiple reflections between crevasse walls causing more melting compared to a smooth ice surface. This aspect of the Jakobshavn Effect was studied by Pfeffer and Bretherton (1987). Meltwater refreezing onto cold crevasse walls releases latent heat that warms ice to the depth of crevasses and thereby accelerates creep rates in ice. As water fills crevasses, it pushes apart crevasse walls and can eventually reach the bed, where it enhances ice motion by drowning bedrock bumps that penetrate basal ice and mobilizes basal till by super-saturation. Zwally et al. (2002) observed this aspect of the Jakobshavn Effect in the ablation zone of the Greenland Ice Sheet a short distance from Jakobshavn Isbrae. However, Schoof (2010) showed theoretically the speedup was short lived and led to a reorganization of the subglacial water drainage system in which ice flow velocity decreases and additional basal meltwater does not increase the veloc-

TCD
8, 2043–2118, 2014

ity. These processes occur preferentially in ice streams, which then move faster than flanking ice, producing lateral shear zones where ice is weakened by frictional heat and easy glide ice fabrics. This aspect of the Jakobshavn Effect was examined by Raymond et al. (2001) for Whillans Ice Stream in West Antarctica. Once ice becomes afloat in fjords, estuarine circulation brings oceanic heat that causes high basal melting rates. Holland et al. (2008) observed this aspect of the Jakobshavn Effect in Jakobshavn Isfjord. High surface and basal melting rates, combined with creep thinning, can free floating ice from basal pinning points. Prescott and others (2003) measured high melting rates on the floating part of Jakobshavn Isbrae. Here we examine how reduced ice-bed coupling under an ice stream and reduced ice-shelf buttressing beyond the ice stream contribute to the Jakobshavn Effect, using recent data from Byrd Glacier in Antarctica (Stearns et al., 2008) and Jakobshavn Isbrae in Greenland (Thomas, 2004), and new maps of surface and bed topography along these ice streams provided by the Center for Remote Sensing of Ice Sheets (CReSIS) at the University of Kansas, using radar sounding.

Since the end of the Little Ice Age in Greenland, about 1850, the ice-sheet margin has ended mostly on land in the south, occupies the inner parts of fjords in the center, and occupies the outer part of fjords in the north. As climate continues to warm, the Jakobshavn Effect is likely to migrate northward, eventually exposing the whole Greenland Ice Sheet to these positive feedback mechanisms. Many ice streams on the east, west, and northwest coasts of Greenland show signs of the Jakobshavn Effect (Rignot and Kanagaratnam, 2006).

Modeling approaches range from the simple Shallow-Ice and Shelfy-Stream Approximations such as IcEIS, UMISM, SICOPOLIS, PISM, and PenState3D (Saito and Abe-Ouchi, 2005; Fastook and Prentice, 1994; Greve, 1997; Bueler and Brown, 2009; Pollard and DeConto, 2012) to higher-order Blatter-Pattyn treatments such as ISSM and CISM 2.0 (Blatter, 1995; Pattyn, 2003; Larour et al., 2012; Bougamont et al., 2011), and on to the computationally-intensive Full–Stokes solutions where no stresses are neglected in the equilibrium equations, see Sargent and Fastook (2010) and results for Elmer/ICE (Seddik et al., 2012). Our alternative treatment provided here is holistic in the sense it provides continuity from sheet flow to stream flow to shelf flow. It relies primarily on a force balance, so our results cannot be used to predict long-term behavior of these ice streams. Our approach uses ice-bed coupling as the major contributor to ice thickness, which we measure directly by radar sounding. This avoids using partial differential equations and continuum mechanics that combine the force, mass, and energy balance. Our mass balance is simple, and our measured ice thicknesses determine the strength of ice-bed coupling directly, which is the main goal of using the energy balance to calculate ice temperatures and basal freezing or melting rates.

The primary research contribution presented here is ice surface, ice thickness, and bed profiles along the centerlines of Byrd Glacier and Jakobshavn Isbrae, profiles extracted from gridded radar-sounding flights in the map plane for these ice streams and for ice converging on these ice streams. We then use measured ice thicknesses to determine the strength of ice-bed coupling for slow sheet flow, fast stream flow, and buttressing shelf flow, thereby obtaining holistic transitions between these flow regimes.

Figure 1 illustrates the challenge we faced. It is a dynamic map of ice-stream tributaries draining the Antarctic ice sheet and converging on major ice streams to supply large buttressing ice shelves (Rignot et al., 2011). What has been called “slow sheet flow” in the interior is better described as tributaries of faster flow imbedded in an overall regime of slower flow. This pattern invites the assumption that a thawed bed predominates along tributaries and a frozen bed predominates between tributaries. “Fast stream flow” is seen as spanning a broad spectrum of ice streams having various sizes and shapes that discharge at least 90 % of Antarctic ice. “Buttressing shelf flow” occurs along margins of the largely marine West Antarctic Ice Sheet, and marine portions of the East Antarctic Ice Sheet. We treat these three flow regimes separately, and then combine them holistically to quantify the Jakobshavn Effect applied to Byrd Glacier in Antarctica and to Jakobshavn Isbrae in Greenland. Summer melting on Byrd Glacier is insufficient to reach the bed to uncouple it from basal ice, and the Ross Ice Shelf buttressing Byrd Glacier is unlikely to disintegrate rapidly. Neither of these con-

cc BY

straints exists for Jakobshavn Isbrae. These considerations guided the conclusions we reached.

2 Ice-bed uncoupling for sheet flow

Ice-bed uncoupling begins with slow sheet flow from interior ice divides that converges on fast stream flow that supplies buttressing ice shelves. The strength of ice-bed coupling determines the first-order ice elevation above the bed. Uncoupling for slow sheet flow begins when a frozen bed thaws. A frozen bed is expected for thin ice along interior ice divides above subglacial highlands. Tributaries should then begin as thawed patches that gradually become linked as ice flows over a largely frozen bed. A thawed bed is expected for thick ice when the ice divide is above a subglacial basin. In this case, tributaries develop over a largely thawed bed. Rignot et al. (2011) take velocities over $50\,\mathrm{m\,a^{-1}}$ as distinguishing faster tributaries imbedded in slower sheet flow. We use thawed fraction f of the bed to quantify ice-bed uncoupling for sheet flow along ice flowlines, with $f \geq 0.6$ for tributaries and $f \leq 0.4$ between tributaries, assuming thawed parts of the bed are connected along flow when $f > 0.5$ and disconnected for $f < 0.5$ to account for the $50\,\mathrm{m\,a^{-1}}$ difference. An earlier approach assumed a mosaic of thawed and frozen patches, with $f = 1$ in thawed patches and $f = 0$ in frozen patches to map thawed, freezing, melting, and frozen zones on the bed (Denton and Hughes, 1981, Chapter 5; Hughes, 1998, Chapters 3, 5, and 9; Wilch and Hughes, 2000; Hughes, 2012, Chapter 24). Ice flow toward Byrd Glacier begins at an ice divide connecting Dome Argus, where thin ice overlies Gamburtsev Subglacial Mountains and probably has a frozen bed, to Dome Circe, where thick ice overlies Wilkes Subglacial Basin and a thawed bed is possible (Drewry, 1983). We selected a flowline beginning at Dome Argus. Since tributaries converge on ice streams, flow from Dome Argus would then cross a melting bed characterized by f in the map plane gradually increasing from $f = 0$ under Dome Argus to $f = 1$ at the head of Byrd Glacier, see Fig. 1. Sheet flow of ice to

CC BY

Jakobshavn Isbrae also probably crosses a melting bed, since it begins at an interior ice dome where ice is frozen to the bed (Gow et al., 1997).

We treated sheet flow along ice flowlines in the downslope direction normal to ice elevation contour lines. In the simplest treatment, the force balance along a flowline balances gravitational force $1/2P_\mathrm{I}h_\mathrm{I}$ against basal drag force $\tau_\mathrm{O}x$ at horizontal distance x from the ice-sheet margin for basal shear stress τ_O, where $1/2\ P_\mathrm{I} = 1/2\rho_\mathrm{I}gh_\mathrm{I}$ is the average ice pressure in ice of height h_I above the bed for gravity acceleration g and ice density ρ_I. Balancing forces gives a parabolic surface profile above a horizontal bed for constant τ_O as a first-order approximation (Nye, 1952a):

$$x = 1/2(\rho_\mathrm{I}g/\tau_\mathrm{O})h_\mathrm{I}^2 \tag{1}$$

Actually, τ_O and bed topography vary along x. These variations are included by differentiating Eq. (1) and solving for surface slope $\alpha = \mathrm{d}h/\mathrm{d}x = \tau_\mathrm{O}/\rho_\mathrm{I}gh_\mathrm{I}$ when ice elevation h a.s.l. differs from ice elevation h_I above the bed, and replacing $\mathrm{d}h/\mathrm{d}x$ with change Δh in constant incremental length Δx between steps i and $i+\mathrm{I}$:

$$h_{i+\mathrm{I}} = h_i + [(\tau_\mathrm{O}/h_\mathrm{I})_i/\rho_\mathrm{I}g]\Delta x = [\tau_\mathrm{O}/(h-h_\mathrm{B})]_i\Delta x/\rho_\mathrm{I}g \tag{2}$$

where τ_O and h_I are specified at each Δx step for integers i. Equation (2) allows variable τ_O and bed topography $h_\mathrm{B} = h - h_\mathrm{I}$ above (+) and below (−) sea level along the flowline, which we measured by radar sounding for Byrd Glacier and Jakobshavn Isbrae. The bed is approximated by an up-down staircase, with $\alpha = (h_{i+1} - h_i)/\Delta x = \Delta h/\Delta x = \Delta h_\mathrm{I}/\Delta x$ on steps and changes $\pm h_\mathrm{B}$ put between steps. When terrestrial ice margins are on broad rather flat plains, Eq. (1) can be used to obtain height h_O at distance x from the ice margin where $i = 0$ in Eq. (2).

Equation (2) is an initial-value, finite-difference recursive formula. Initial ice elevation h_O above the bed must be specified at $i = 0$ in order to start the boot-strapping process of calculating $h_\mathrm{I} = h - h_\mathrm{B}$ along the flowline at each i step. Present-day values of h_B can be adjusted to account for isostatic depression and rebound of the bed during a glaciation cycle (Hughes, 1998, Chapter 5; Hughes, 2012, Chapter 22). This adjustment is not necessary in our study using only present-day conditions.

Ice shearing over a frozen bed has basal shear stress τ_F that is higher than basal shear stress τ_S for ice sliding over a thawed bed or for shearing water-saturated till between basal ice and bedrock, owing to reduced ice-bed coupling when the bed thaws. Thawing lowers the ice surface. Thawed fraction f then gives:

$$\tau_O = f\tau_S + (1 - f)\tau_F = \rho_I g h_I \alpha \tag{3}$$

Expressions for τ_F and τ_S can be provided by respective flow laws and sliding laws for ice (Denton and Hughes, 1981, Chapter 5; Hughes, 1998, Chapters 3 and 5; Hughes, 2012, Chapter 17). For sheet flow in the Antarctic Ice Sheet, $0.25 \leq f \leq 0.75$ is widespread, with $f = 0$ common under ice domes over subglacial highlands and $f = 1$ common under ice domes over subglacial basins and at the heads of ice streams entering deep fjords (Hughes, 1998, Chapter 3; Hughes, 2012, Chapter 24; Wilch and Hughes, 2000).

Flow and sliding laws give vertically averaged ice velocities and basal sliding velocities, respectively, with the basal sliding velocity only slightly less than the ice surface velocity owing to reduced basal drag on a thawed bed. These velocities are used in a mass-balance equation to calculate ice elevations above the bed along flowlines using Eq. (3) for thawed fraction f to evaluate τ_O in Eq. (2). In original theories of basal sliding, sliding velocity depends on melting and freezing rates of ice on the stoss and lee sides of bedrock bumps, and on high-stress creep rates around bumps (Weertman, 1957a), and also on an "effective" basal water pressure (Lliboutry, 1968). Till deformation of West Antarctic ice streams appears to be nearly viscous, based on field measurements (Anandakrishnan and Alley, 1997), or nearly plastic, based on laboratory experiments (Kamb, 2001), conducted on the same till, let alone on different tills. Given ambiguities in deformation studies for glacial sliding over bedrock and till shearing between basal ice and bedrock, we propose a different approach in this study based on using separate yield stresses for creep in ice and for basal sliding with till deformation. These ambiguities arise from the extreme variability of ice and till near the bed of West

cc BY

Antarctic ice streams, as documented in detail for Kamb Ice Stream (formerly ice steam C) by Engelhardt and Kamb (2013).

Since till can deform near both the viscous and plastic ends of the viscoplastic creep spectrum, and presumably anywhere in between, depending on variable mineral compositions, lithological textures, and water content, quantifying creep in till must allow this range. We measured h_I and α directly using radar sounding, so values of f in Eq. (3) can be calculated using specified values of τ_S and τ_F for given values of n in Fig. 2.

Figure 2 shows the viscoplastic creep spectrum for crystalline and composite materials (Hughes, 1998, Chapter 9). The creep equation is:

$$\dot{\varepsilon} = \dot{\varepsilon}_\mathrm{O}(\sigma/\sigma_\mathrm{O})^n \quad (4)$$

where $\dot{\varepsilon}$ is the strain rate caused by applied stress σ, the plastic yield stress is σ_O, the viscoplastic creep exponent is n, and $\dot{\varepsilon}_\mathrm{O}$ is the strain rate when $\sigma = \sigma_\mathrm{O}$ for all values of n over the range $1 \le n \le \infty$. For viscous flow when $n = 1$, the viscosity is $\eta = \sigma/\dot{\varepsilon}$ and yield stress $\sigma_\mathrm{O} = 0$. For plastic flow when $n = \infty$, viscosity $\eta = \infty$ when $\sigma < \sigma_\mathrm{O}$ and $\eta = 0$ when $\sigma = \sigma_\mathrm{O}$. In between, a viscoplastic yield stress σ_V and a viscoplastic viscosity $\eta_\mathrm{V} = \mathrm{d}\sigma/\mathrm{d}\dot{\varepsilon}$ must be specified. For glacier ice, $n = 3$ is typical. Two values of σ_V and η_V can be imagined, and are shown in Fig. 2. In the critical strain-rate yield criterion, values at $\dot{\varepsilon}_\mathrm{O}$ are η_V as the slope of the line tangent to the curve and σ_V is the stress-intercept of the tangent line. In the critical shear-stress yield criterion, σ_V is the point on the curve where stress curvature is a maximum and η_V is the slope of the line tangent to this point on the curve. These two yielding criteria were originally proposed for nucleation and propagation, respectively, of cracks leading to crevasse formation and calving of icebergs (Hughes, 1998, Chapter 8). We assume these two values for till as well, before and after the ice fraction in till melts.

For ice to slide over bedrock or for till to be mobilized, sensible and latent heat must be provided to warm and melt ice that contacts bedrock or ice that cements basal till. Basal heat is provided by geothermal heat and frictional heat produced by deforming ice. Per unit volume of ice, frictional heat is the product of the shear stress and the shear strain rate (Paterson, 1994), so viscoplastic yield stress σ_V is defined by $\dot{\varepsilon}_O$ at all values of n just before melting takes place, with $\sigma_V = 0.667\sigma_O$ for $n = 3$. After basal ice in contact with bedrock or in ice-cemented till melts, basal sliding and till deformation become possible and are concentrated at the ice–bed interface where u_O is the ice velocity. Then the creep rate does not depend on $\dot{\varepsilon}_O$ and prevails because heat generated by deforming unit area of basal ice is the product of u_O and σ_V, with $\sigma_V = 0.386\sigma_O$ for $n = 3$. The energy needed to provide latent heat of melting is not required, so a lower stress and strain rate are allowed, compared to frozen-bed conditions. This, of course, is an assumption of convenience to avoid dealing with poorly known basal deformation processes. It should be abandoned when these processes are fully quantified.

As an approximation for ice, $\sigma_O = 100\,\text{kPa}$ is commonly taken (Paterson, 1994). Then in Eq. (3), $\tau_F = \sigma_V = 66.7\,\text{kPa}$ for ice creeping above a frozen bed and $\tau_S = \sigma_V = 38.6\,\text{kPa}$ for ice sliding above a thawed bed or for mobilized till. The gravitational driving stress for sheet flow in the Antarctic Ice Sheet, where Eq. (3) applies if a mosaic of frozen and thawed areas exists on the bed, is commonly 45 to 55 kPa (e.g., Budd et al., 1971; Drewry, 1983). These values lie between the 38.6 and 66.7 kPa limits for viscoplastic yield stress σ_V in Fig. 2 postulated here for temperate ice moving over a thawed bed or till and for generally colder ice moving over a frozen bed or till, respectively applied to ice in tributaries and to ice between tributaries in our treatment here.

Following Hughes (1998, Chapter 9), if thawing of a frozen bed begins in hollows between hills, so the bed becomes a mosaic of frozen and thawed patches, thawed patches will move up hills until the whole bed is thawed. Conversely, if a thawed bed becomes frozen first on hills, frozen patches will move into hollows until the whole bed is frozen. This rolling bed topography typically developed before glaciation when fluvial processes produced a dendritic pattern of small streams supplying large rivers. Therefore, the thawed patches should lengthen in the direction of ice flow and become tributaries that supply major ice streams, as shown dramatically by Rignot et al. (2011)

cc BY

for the Antarctic Ice Sheet, see Fig. 1. Their results are consistent with this way of linking thawed areas to bed topography and even subglacial lakes in applying Eq. (3), see Wilch and Hughes (2000), Siegert (2001), and Smith et al. (2009). This linkage provides the means for converting slow sheet flow into fast stream flow.

Gravitational spreading during sheet flow is resisted primarily by basal drag, so the dominant resisting stress σ_{xz} produces strain rate $\dot{\varepsilon}_{xz} = \partial u_x/\partial z$ for ice velocity u_x when x is horizontal distance in the downslope direction of ice flow and z is vertical distance above the bed. The flow law of ice for this case is (Glen, 1958):

$$\dot{\varepsilon}_{xz} = \dot{\varepsilon}_{\mathrm{O}}(\sigma_{xz}/\sigma_{\mathrm{O}})^n = (\sigma_{xz}/A)^n \tag{5}$$

where $A = \sigma_{\mathrm{O}}/\dot{\varepsilon}_{\mathrm{O}}^{1/n}$ is an ice hardness parameter that depends on the fabric of polycrystalline ice and ice temperature. Basal drag produces an easy-glide ice fabric in ice near the bed in which the optic axes of ice crystals tend to be normal to the bed, and produces frictional heat that makes ice warmer toward the bed.

Following Hughes (2012; Appendix O), for constant A the vertical profile of horizontal ice velocity is obtained by integrating Eq. (5):

$$u_x = 2(\rho_{\mathrm{I}} g\alpha/A)^n \left[h_{\mathrm{I}}^{n+1} - (h_{\mathrm{I}} - z)^{n+1}\right]/(n+1) \tag{6}$$

for which the vertically averaged horizontal ice velocity is:

$$\overline{u_x} = [2h_{\mathrm{I}}/(n+2)](\rho_{\mathrm{I}} g h_{\mathrm{I}}\alpha/A)^n = [2h_{\mathrm{I}}/(n+2)](\tau_{\mathrm{O}}/A)^n \tag{7}$$

Then the ratio of $\overline{u_x}$ to u_x at $z = h_{\mathrm{I}}$ is $(n+1)/(n+2)$, which is $2/3$ for $n = 1$, $4/5$ for $n = 3$, and $51/52$ for $n = 50$. Since A is kept constant, the reduction of A near the bed due to development of an easy-glide ice fabric and the increase of ice temperature must be represented by an increase in n greater than $n = 3$ commonly obtained for creep experiments on ice samples using stresses of about one bar (100 kPa) typical for ice

TCD
8, 2043–2118, 2014
Quantifying the Jakobshavn Effect
T. Hughes et al.

sheets (Paterson, 1994). For ice accumulation rate a and ice thinning rate r averaged along x:

$$A = \left[4\tau_O^{n+1}/(n+2)\rho_I g(a-r)\right]^{1/n} \tag{8}$$

The dependence of A on $(a-r)$ quickly becomes insignificant as n increases and $A \to \tau_O$. For typical flowlines 1500 km long on the East Antarctic Ice Sheet, take $\rho_I = 917\,\mathrm{kg\,m^{-3}}$, $g = 9.8\,\mathrm{m\,s^{-2}}$, $h_I = 3\,\mathrm{km}$, $\alpha = 0.002$, and $(a-r) = 0.1\,\mathrm{m\,a^{-1}}$. Then $\tau_O = \rho_I g h_I \alpha = 54 \times 10^3\,\mathrm{kg\,m^{-1}\,s^{-2}} = 54\,\mathrm{kPa}$, which lies between $\tau_F = 66.7\,\mathrm{kPa}$ and $\tau_S = 38.6\,\mathrm{kPa}$ in Eq. (3). This indicates that sheet flow occurs over a bed that is partly frozen and partly thawed to allow sliding of ice.

Since Rignot et al. (2011) took a surface velocity change of $50\,\mathrm{m\,a^{-1}}$ in and between tributaries, we take $u_x = 75\,\mathrm{m\,a^{-1}}$ in tributaries and $u_x = 25\,\mathrm{m\,a^{-1}}$ between tributaries for sheet flow as typical. Referring to Fig. 2, we then calculate A from Eq. (6) using u_x at $z = h_I$ for the surface velocity when $n = 1$ for viscous flow, $n = 3$ for ice flow, and $n = 50$ for plastic flow. For $u_x = 75\,\mathrm{m\,a^{-1}}$ in tributaries, $A = 6.8 \times 10^{13}\,\mathrm{kg\,m^{-1}\,s^{-1}}$ when $n = 1$, $A = 4.6 \times 10^7\,\mathrm{kg\,m^{-1}\,s^{-2+1/3}}$ when $n = 3$, and $A = 7.7 \times 10^4\,\mathrm{kg\,m^{-1}\,s^{-2+1/50}}$ when $n = 50$. For $u_x = 25\,\mathrm{m\,a^{-1}}$ between tributaries, $A = 2.0 \times 10^{14}\,\mathrm{kg\,m^{-1}\,s^{-1}}$ when $n = 1$, $A = 6.7 \times 10^7\,\mathrm{kg\,m^{-1}\,s^{-2+1/3}}$ when $n = 3$, and $A = 7.9 \times 10^4\,\mathrm{kg\,m^{-1}\,s^{-2+1/50}}$ when $n = 50$. For both values of u_x, $A \approx 1.4 \times 10^{14}\,\mathrm{kg\,m^{-1}\,s^{-1}} = 1.4 \times 10^{15}$ poise for $n = 1$, $A \approx 5.6 \times 10^7\,\mathrm{kg\,m^{-1}\,s^{-5/3}}$ for $n = 3$, and $A \approx 7.8 \times 10^4\,\mathrm{kg\,m^{-1}\,s^{-2+1/n}} = 40\,\mathrm{kPa}$ when $n \geq 50$. Velocity profiles of u_x vs. z for these three values of A are plotted in Fig. 3 from Eq. (6). As n increases, A is increasingly independent of n, with u_x becoming almost constant through h_I except very near the bed, and $\overline{u_x}$ gets closer to the surface velocity, all signifying increasing ice-bed uncoupling. For $n > 50$, ice velocity becomes virtually constant through h_I as n increases, with velocity increases confined to ice sliding over wet deforming till at the bed. This is the condition for a thawed bed, and occurs in ice tributaries.

In Fig. 3, the velocity profile for $n = 50$ is nearly linear close to the bed where a till layer may exist. A linear profile for till is obtained by setting $\dot{\varepsilon}_{xz} = \mathrm{d}u_x/\mathrm{d}z$ and $\sigma_{xz} = \tau_V$ in Eq. (5). Then $u_x = (\tau_V/A)^n z$ for constant τ_V and A in the till layer for all n values.

We could use any value of n in Fig. 2 and the corresponding values of τ_S and τ_F to calculate f in Eq. (3). However, values of τ_O obtained from our measured values of h_I and α using radar sounding are most compatible with $\tau_S = 38.6$ kPa and $\tau_F = 66.7$ kPa for $n = 3$. This means our value of A calculated from Eq. (8) is vertically averaged through h_I. We could use separate values of n for thawed ($n > 50$) and frozen ($3 < n < 50$) beds for $f = 1$ in tributaries and $f = 0$ between tributaries, and use the corresponding values of A, but the choice would be arbitrary, and makes Eq. (3) useless. Figure 1 then becomes a map of places where $f = 1$ (tributaries) and $f = 0$ (between tributaries), which may be approximately the case, but isolated thawed patches can exist between tributaries.

It should be mentioned that $n > 50$ might apply if ice flows over a rugged bed consisting of riegels on a scale of 100 m or so. Rowden-Rich and Wilson (1996) maintained that the an ice sheet would then produce its own smooth bed by developing a zone of intense shear over the tops of riegels, and applied that concept to flow from Law Ice Dome in East Antarctica. The complex pattern of tributaries in Fig. 1 would seem to preclude that possibility. However, it emphasizes the need to measure velocity profiles in the field. Our study would benefit greatly if we had such data for Byrd Glacier and Jakobshavn Isbrae in our treatment of stream flow, where that mechanism is more probable.

3 Ice-bed uncoupling for stream flow

Ice streams develop from their tributaries when basal meltwater progressively drowns bedrock bumps that penetrate basal ice and supersaturates till in directions of ice flow. This occurs when $f = 1$, so additional melting must thicken the basal water layer, rather than increase its areal extent, and must supersaturate subglacial till. Then floating frac-

cc BY

tion φ replaces thawed fraction f along flowlines. A geometrical force balance combines with a simple mass balance to calculate h_I based on the formula (Hughes et al., 2011; Hughes, 2012, Chapter 10):

$$\varphi = h_\mathrm{F}/h_\mathrm{I} \tag{9}$$

where h_F is the height (thickness) of ice that floats in water. It is related to basal ice area A_F that floats in given basal area A_O so that $\varphi = A_\mathrm{F}/A_\mathrm{O}$ because h_F is adjusted until $h_\mathrm{F}A_\mathrm{O} = h_\mathrm{I}A_\mathrm{F}$ are volumes of ice that exert the same vertical gravitational force on the bed. At a point having zero basal area, height h_F is still determined by $A_\mathrm{F}/A_\mathrm{O}$ in the immediately surrounding basal area, see Fig. 4. This condition exists under West Antarctic ice streams (Fricker and Scambos, 2009; Engelhardt and Kamb, 2013).

A holistic ice-sheet model must provide smooth transitions from sheet flow to stream flow to shelf flow for the longitudinal force balance in the direction of gravitational flow of ice, a task now accomplished by continuum models (e.g., Pattyn, 2003; Sargent, 2009; Sargent and Fastook, 2010; Blatter et al., 2011). If this force balance is done for flowbands having the width of an ice stream, assumed to be constant, the six resisting stresses in the equilibrium equations reduce to four, a longitudinal tension stress σ_T that pulls upslope ice, a longitudinal compression stress σ_C that pushes downslope ice, a basal shear stress τ_O due to basal drag, and a side shear stress τ_S due to side drag. Transverse stresses caused by converging and diverging flow that changes the flowband width can then be ignored in the essentially one-dimensional solutions presented here. This allows a force balance based on simple geometry in the longitudinal direction of ice flow, along which all of these stresses vary with changing floating fraction φ of ice in the flowband. This is a visual approach, with forces represented by geometrical areas. Partial differential equations such as the equilibrium equations are avoided. For sheet flow, $\varphi = 0$ when the bed is dry (frozen) and $\varphi \to 0$ when the bed is wet (thawed). For stream flow, $0 < \varphi < 1$ with φ often increasing downstream. For shelf flow, $\varphi = 1$ for a freely-floating ice shelf and $\varphi \to 1$ when a confined and locally pinned ice shelf buttresses the ice stream.

TCD
8, 2043–2118, 2014

cc BY

Figure 4 is a cartoon showing places where $\varphi = 0$ for ice grounded on a wet bed under an ice stream, and $\varphi = 1$ for places where ice floats in water under the ice stream. Hughes (2012, Chapter 10) assumed these places generally correspond to hills and hollows in bedrock topography, or to soft sediments or till that are unsaturated and supersaturated with water, respectively. Bedrock hills and unsaturated till resist gravitational motion. Taking Cartesian coordinates with x horizontal and positive against ice flow, y horizontal and transverse to ice flow, and z vertical and positive a.s.l., at distance x from the ice-shelf grounding line, a flowband of width w_I has floating segments that add up to width $w_F < w_I$ in the ice stream. Floating fraction φ defined by Eq. (9) is linked to the horizontal longitudinal force-and-mass balance at x using this elaboration:

$$\varphi = \frac{w_F}{w_I} = \frac{h_F}{h_I} = \frac{(\rho_W/\rho_I)h_W}{h_I} = \frac{\rho_W g h_W}{\rho_I g h_I} = \frac{P_W^*}{P_I} \tag{10}$$

where $h_F = h_I\,(w_F/w_I) = h_I\varphi$ is the part of ice thickness h_I supported by basal water, ρ_W is water density, ρ_I is ice density, h_W is an effective water depth that would float thickness h_F of ice, P_W^* is an effective basal water pressure that is caused by h_W and increases as basal drag resisting ice flow decreases, P_I is the ice overburden pressure, and g is gravity acceleration. In a vertical force balance, apply Newton's second and third laws of motion to the base of columns having basal area $A_O = w_I \Delta x$. Gravity forces $\rho_I g h_I A_O$ and $\rho_W g h_W A_O$ are balanced by pressure forces $P_I A_O$ and $P_W A_O$, respectively, giving $P_W = \rho_W g h_W$ as the actual basal water pressure and $P_I = \rho_I g h_I$ as the basal ice pressure. For ice shelves, $P_W = P_I$ everywhere. For ice streams $P_W \approx P_I$ because basal water flowing from sources to sinks causes variations in P_W that do not coincide everywhere with P_I. Taking $\sigma_W h_I = \overline{P_W^*} h_W$ in a longitudinal force balance introduces back-stress σ_W in ice due to $\overline{P_W^*} = 1/2 P_W^*$ that resists ice motion, where $P_W^* < P_W$ at $x > 0$ under an ice stream and $P_W^* = P_W$ at $x = 0$ under an ice shelf, see Fig. 5. At the calving front water is in direct contact with a vertical ice cliff and $\sigma_W = 1/2 P_W (h_W/h_I)$ in the longitudinal force balance.

TCD
8, 2043–2118, 2014
Quantifying the Jakobshavn Effect
T. Hughes et al.

CC BY

Figure 5 shows an exaggerated vertical longitudinal cross-section of a flowband from the ice divide to an ice stream and ending at the calving front of a confined and pinned ice shelf. Flow is from right to left. The top panel shows in shading the part of the flowband that rests on the bed. Solid, broken, and dashed lines show respective heights h_I, h_F, and h_W above basal ice. The ice shelf lies in a confining embayment grounded along side lengths L_S, at an ice rise of circumference C_R, and at ice rumples of area A_R, so it buttresses the ice stream. Stresses resisting gravitational flow are σ_T, σ_C, τ_O, and τ_S shown at distance x from the ice-shelf grounding line, and $\overline{\tau_\mathrm{O}}$ and $\overline{\tau_\mathrm{S}}$ averaged over the distance from 0 to x.

The middle panel shows a large triangular area equal to gravitational driving force $1/2P_\mathrm{I}h_\mathrm{I}$. Within that triangle are areas linked to resisting forces, with the area inside the bold border linked to compressive force $\sigma_\mathrm{C}h_\mathrm{I}$ and the remaining small triangular area linked to tensile force $\sigma_\mathrm{T}h_\mathrm{I}$. This force balance gives:

$$1/2P_\mathrm{I} = \overline{P_\mathrm{I}} = \sigma_\mathrm{C} + \sigma_\mathrm{T} \tag{11}$$

Note that $\sigma_\mathrm{C} \gg \sigma_\mathrm{T}$ because area $1+2+3$ enclosed by the bold border greatly exceeds triangle area 4, so a minor downslope decrease in resistance to ice flow causes a small decrease in σ_C but a large increase in σ_T because P_I is initially unchanged. This shows how σ_T can pull more ice out of ice sheets for only a small decrease in downslope resistance to ice flow (Hughes, 1992).

The bottom panel equates areas 1, 2, and 3 with compressive force $\sigma_\mathrm{C}h_\mathrm{I}$, triangular area 4 to tensile force $\sigma_\mathrm{T}h_\mathrm{I}$, triangular area 3 to water-buttressing force $\sigma_\mathrm{W}h_\mathrm{I}$, area $3+4$ to flotation force $\sigma_\mathrm{F}h_\mathrm{I}$, the difference between triangular areas 5 and 4 to basal drag force $\tau_\mathrm{O}\Delta x$, and the difference between rectangular areas 6 and 2 to side drag force $2\tau_\mathrm{S}\Delta x$ for two sides. Balancing these longitudinal forces as $\Delta x \to 0$ gives (Hughes, 2009; Hughes, 2012, Appendix G):

$$\sigma_\mathrm{T} = 1/2\rho_\mathrm{I}gh_\mathrm{I}(1-\rho_\mathrm{I}/\rho_\mathrm{W})\varphi^2 = \overline{P_\mathrm{I}}(1-\rho_\mathrm{I}/\rho_\mathrm{W})\varphi^2 \tag{12}$$

$$\sigma_\mathrm{C} = 1/2\rho_\mathrm{I}gh_\mathrm{I}\left[1-(1-\rho_\mathrm{I}/\rho_\mathrm{W})\varphi^2\right] = \overline{P_\mathrm{I}}\left[1-(1-\rho_\mathrm{I}/\rho_\mathrm{W})\varphi^2\right] \tag{13}$$

$$\sigma_W = 1/2\rho_I g h_I(\rho_I/\rho_W)\varphi^2 = \overline{P}_I(\rho_I/\rho_W)\varphi^2 \quad (14)$$

$$\sigma_F = \sigma_T + \sigma_W = \overline{P}_I\varphi^2 \quad (15)$$

$$\tau_O = 1/2\rho_I g h_I(1-\varphi)\left[\alpha_I - \partial(h_I\varphi)/\partial x\right] = P_I(1-\varphi)^2\alpha \quad (16)$$

$$\tau_S = 2\rho_I g h_I(w_I/h_I)\left[\varphi\alpha_I - (1-2\varphi)\partial(h_I\varphi)/\partial x\right] \rightarrow P_I(w_I/h_I)\varphi(1-\varphi)\alpha \quad (17)$$

$$\partial(\sigma_F h_I)/\partial x = \partial(\sigma_T h_I)/\partial x + \partial(\sigma_W h_I)/\partial x = P_I(\rho_I/\rho_W)\varphi\alpha_W \quad (18)$$

Here $\Delta h/\Delta x \rightarrow \alpha$ is the ice surface slope, $\Delta h_I/\Delta x \rightarrow \alpha_I$ is the ice thickness gradient, and $\Delta h_W/\Delta x \rightarrow \alpha_W$ is the gradient of basal water height giving effective basal water pressure P_W^* resisting gravitational ice flow as $\Delta x \rightarrow 0$. Water buttressing produces back-stress $\sigma_W = (h_W/h_I)\overline{P_W^*}$ in ice due to $\overline{P_W^*}$ in a longitudinal force balance. Flotation stress σ_F in ice is due to $\sigma_W + \sigma_T$ in the longitudinal force balance $\sigma_F h_I = \sigma_W h_I + \sigma_T h_I$. These are real stresses. They are obscured using holistic continuum mechanics in conventional ice-sheet models, but they visibly emerge from the geometrical force balance in the holistic ice-sheet model based on Fig. 5.

Demonstrating that h_F in Eq. (9) and P_W^* in Eq. (10) are real, and therefore σ_W is real, has been a challenge (Hughes, 1992, 2003, 2011, 2012, Chapter 10; Hughes et al., 2011). Relating h_F to h_I and h_W at the calving front of an ice shelf uses the horizontal longitudinal force balance $\rho_I h_I = \rho_W h_W$ because heavier water of height h_W buttresses lighter ice of height h_I, so $h_F = h_I = (\rho_W/\rho_I)h_W$. That this is also true at an ice-shelf grounding line is not so obvious, the objection being that ice of reduced thickness buttresses ice on the forward side of an ice column to produce a concave ice-thickness profile first calculated by Sanderson (1979), then by van der Veen (1983). A rigorous force balance includes buttressing from the wedge of water under the ice column anywhere between the calving front and the grounding line (Hughes, 2012, Chapter 9). Apart from this rigorous force balance, an obvious demonstration is to melt the ice shelf so water buttresses ice at the grounding line just as it did at the calving front.

TCD
8, 2043–2118, 2014

Having overcome that objection for the grounding line, the objection is still maintained that it cannot apply up an ice stream that also has a concave profile (G. Robin, personal communication, 1988; D. Pollard, personal communication, 2007). How can h_W in Fig. 5 "buttress" an ice stream at distance x upstream from the ice-shelf grounding line when there is no water of height h_W at x? This confuses the distinction between a vertical force balance and a longitudinal (horizontal) force balance. Height h_W acts like water impounded by a "dam" that exists because downstream resistance to water flowing under an ice stream exists. It is similar to resistance from a laterally confined and locally pinned ice shelf that causes h_W to be greater and gradient $\partial h_W/\partial x$ to be less at the grounding line than they would be for a freely-floating ice shelf. The "obvious" demonstration of this is the height of water in boreholes drilled by Barclay Kamb and Hermann Engelhardt along Whillans Ice Stream: the water height above the bed was well a.s.l. and somewhat below the height needed to float ice thickness h_I, so $h_F < h_I$ as shown in Fig. 5, see Kamb (2001). However it is not "obvious" this validates Eq. (10). Mean effective water pressure $\overline{P_W^*}$ "buttresses" ice in the longitudinal force balance that produces a "water" back-stress σ_W in ice of height h_I above the bed. MacAyeal (1989) modeled Whillans Ice Stream as a linear ice shelf with some basal drag. His analytical force balance is not so different conceptually from the geometrical force balance introduced for ice streams by Hughes (1992) and illustrated in Fig. 5, where the analytical flaws are avoided by using geometry.

The distinction between P_W^* in Eq. (10) and P_W is that $P_W \approx P_I$ vertically when the bed is wet, but $P_W^* < P_I$ horizontally in proportion to $A_W < A_O$ for ice floating over basal area $A_F = A_W$ within basal area A_O. Where Kamb and Engelhardt drilled through Whillans Ice Stream, A_W wasn't much less than A_O.

The longitudinal force balance pits gravitational driving force gradient $\Delta(\overline{P}_I h_I)/\Delta x = P_I \alpha$ as $\Delta x \to 0$, obtained from the difference between area $5+6+7+8$ and area $1+2+3+4$ in incremental length Δx in Fig. 5, against resisting stresses τ_O and τ_S and

CC BY

flotation force gradient $\partial(\sigma_F h_I)/\partial x$ to obtain (Hughes, 2011, 2012, Appendix G):

$$P_I \alpha = \tau_O + 2\tau_S (h_I/h_W) + \partial(\sigma_F h_I)/\partial x \tag{19}$$

Equation (19) is satisfied using substitutions from Eqs. (16)–(18).

Now approximate bed topography with an up-down staircase in which Δx is the constant step length and $\pm\Delta h_B$ is the variable gain or loss in step height. A normal stress σ_N in the direction of ice flow pushes against $-\Delta h_B$ and pulls away from $+\Delta h_B$ with force $F_N = \pm\sigma_N \Delta h_B$ compared to gravitational driving force $F_G = \overline{P_I} h_I$, so that $\sigma_N \Delta h_B/\Delta x$ and $P_I \Delta h/\Delta x$ are force gradients with σ_N close to viscoplastic yield stress σ_V in Fig. 2. Then F_N is much less than F_G until the bed slope exceeds $\pm 30^\circ$ (Hughes, 2012, Appendix E), so F_N can be ignored for lesser bed slopes. Then $\Delta h = \Delta h_I$ can be used for each Δx step. Substituting Eqs. (16)–(18) into Eq. (19), putting terms containing $\partial\varphi/\partial x$ between Δx steps, dividing by P_I, solving for surface slope α, and returning to the incremental form so $\partial\varphi/\partial x \approx \Delta\varphi/\Delta x$ and $\alpha \approx \Delta h/\Delta x$:

$$\begin{aligned} \frac{\Delta h}{\Delta x} &= \frac{\Delta(\sigma_F h_I)/\Delta x}{P_I} + \frac{\tau_O}{P_I} - \frac{2\tau_S(h_I/h_W)}{P_I} \\ &= \varphi^2 \left(\frac{\Delta h_I}{\Delta x}\right)_F + (1-\varphi)^2 \left(\frac{\Delta h_I}{\Delta x}\right)_G + 2\varphi(1-\varphi)\left(\frac{\Delta h}{\Delta x}\right) \end{aligned} \tag{20}$$

Here $\Delta h_I = \Delta h$ on Δx steps, so $(\Delta h/\Delta x)_F$ is for the floating fraction of the ice column linked to σ_F and $(\Delta h/\Delta x)_G$ is for the grounded fraction of the ice column linked to τ_O on these steps. Putting $\Delta h_B/\Delta x$ and $\Delta\varphi/\Delta x$ between Δx steps is a major simplification that avoids integrating partial differential equations. If unwarranted, this assumption invalidates everything that follows, see Hughes (2012, Chapter 20, Appendices E and P).

When only the geometrical force balance is used, Eq. (9) becomes (Hughes, 2012, Chapter 11):

$$\varphi = h_O/h_I \tag{21}$$

CC BY

Equation (21) is obtained both for ice streams with side shear and for the central flowline of an ice stream without side shear. In Eq. (21), h_O is ice height above the bed at $x = 0$ where the ice stream becomes a floating ice shelf, so $h_O = h_I$ when $\varphi = 1$ but $\varphi < 1$ at horizontal distances x up the ice stream where $h_O < h_I$. For sheet flow, $\varphi = 0$ because $h_O = 0$ at the ice margin. For shelf flow, $\varphi = 1$ when $h_O = h_I$ everywhere. For stream flow, $1 > \varphi > 0$ because $h_I > h_O$. The mass balance must be combined with the force balance to obtain solutions of φ that satisfy Eq. (9).

A simple mass balance is shown in Fig. 6 for constant ice accumulation rate a and ice thinning rate r along x, with $h_I = h_L$ where ice velocity $u_x = 0$ at the ice divide ($x = L$), $h_I = h_S$ where $u_x = u_S$ and stream flow begins ($x = S$), and $h_I = h_O$ where $u_x = u_O$ at the ice-shelf grounding line ($x = 0$), so that:

$$(a - r)(L - x) = h_I u_x \tag{22}$$

Since a and r can vary along x, Eq. (22) is a simplification comparable to Eq. (20) and, if unwarranted, invalidates everything that follows. Validation requires that φ, h_B, a, and r vary slowly along x.

Here is how $(\Delta h/\Delta x)_G$ is obtained. Assume the bed is thawed in grounded areas $A_G = A_O - A_F$ so grounded ice slides over the bed at velocity u_S. Using a conventional sliding law for ice (Weertman, 1957a), where B includes bed roughness and physical properties of temperate ice at the bed, $m = 2$ for sliding ice, and $u = u_x = u_S$:

$$u = u_S = \left(\frac{\tau_O}{B}\right)^m \tag{23}$$

Equate ice elevation h with ice thickness h_I for a horizontal bed at sea level. Combine Eqs. (22) and (23), with $\tau_O = \rho_I g h_I \mathrm{d}h_I/\mathrm{d}x$ now depending only on the strength of ice-bed coupling linked to grounded thawed fraction $f = 1$ under ice streams:

$$(a - r)(L - x) = h_I u = h_I(\tau_O/B)^m = h_I\left[(\rho_I g h_I/B)\mathrm{d}h_I/\mathrm{d}x\right]^m \tag{24}$$

Now let h_I vary with bed topography, using measured values of h_I in Eq. (24). Solve for surface slope $\alpha = \mathrm{d}h/\mathrm{d}x$:

$$\alpha = \frac{\mathrm{d}h}{\mathrm{d}x} = \frac{B}{\rho_\text{I} g h_\text{I}} \left[\frac{(a-r)(L-x)}{h_\text{I}}\right]^{\frac{1}{m}} \tag{25}$$

Taking $\tau_\text{O} = \rho_\text{I} g h_\text{I} \alpha$ and setting $\alpha = (\Delta h/\Delta x)_\text{G}$ for ice grounded in incremental length Δx, Eq. (25) gives:

$$\left(\frac{\Delta h_\text{I}}{\Delta x}\right)_\text{G} = \frac{\tau_\text{O}}{\rho_\text{I} g h_\text{I}} = \frac{(B/\rho_\text{I} g)[(a-r)(L-x)]^{\frac{1}{m}}}{h_\text{I}^{\frac{m+1}{m}}} \tag{26}$$

Note the weak dependence $h_\text{I} \propto (a-r)^{1/3}$ for $m = 2$. To a first approximation, this "justifies" ignoring slow variations of $(a-r)$ and also of a and r separately along x in Eq. (22).

Calculating $(\Delta h/\Delta x)_\text{F}$ begins with the mass balance in Fig. 6 written as follows:

$$h_\text{I} u_x = h_\text{O} u_\text{O} + (a-r)x \tag{27}$$

Note that velocities u_x and u_O are negative with x positive upslope. Differentiating at point x:

$$\begin{aligned} \partial(h_\text{I} u_x)/\partial x &= \partial[h_\text{O} u_\text{O} + (a-r)x]/\partial x = (a-r) \\ &= u_x \partial h_\text{I}/\partial x + h_\text{I} \partial u_x/\partial x = u_x \partial h_\text{I}/\partial x + h_\text{I} \dot{\varepsilon}_{xx} \end{aligned} \tag{28}$$

where $\dot{\varepsilon}_{xx} = \partial u_x/\partial x$ is the longitudinal strain rate along x. Solve for incremental slope $(\Delta h/\Delta x)_\text{F}$ by setting $u_x = u$ and $\dot{\varepsilon}_{xx} = \dot{\varepsilon}$ with u_x obtained from Eq. (24):

$$\left(\frac{\Delta h}{\Delta x}\right)_\text{F} = \frac{(a-r) - h_\text{I}\dot{\varepsilon}}{u_x} = \frac{h_\text{I}(a-r) - h_\text{I}^2\dot{\varepsilon}}{h_\text{O} u_\text{O} + (a-r)x} \tag{29}$$

TCD
8, 2043–2118, 2014

CC BY

Using the flow law of ice (Glen, 1958), where A is an ice-hardness parameter dependant on temperature and $n = 3$ for ice, $\dot{\varepsilon}_{xx} = \Delta u/\Delta x$ is the extending strain rate for stress σ_T given by Eq. (12) with $\varphi = 1$ for floating ice, and R is a dimensionless scalar that takes account of other strain rates in addition to $\dot{\varepsilon}_{xx}$:

$$\dot{\varepsilon} = \dot{\varepsilon}_{xx} = \Delta u/\Delta x = R\left(\frac{\sigma'_{xx}}{A}\right)^n = R\left(\frac{\sigma_T}{2A}\right)^n \tag{30}$$

where deviator stress $\sigma'_{xx} = 1/2\sigma_T$ for ice streams (Hughes, 2012, Chapter 10). From Hughes (2012, Appendix A):

$$R = \left[1 + \left(\frac{\dot{\varepsilon}_{yy}}{\dot{\varepsilon}_{xx}}\right) + \left(\frac{\dot{\varepsilon}_{yy}}{\dot{\varepsilon}_{xx}}\right)^2 + \left(\frac{\dot{\varepsilon}_{xy}}{\dot{\varepsilon}_{xx}}\right)^2 + \left(\frac{\dot{\varepsilon}_{xz}}{\dot{\varepsilon}_{xx}}\right)^2\right]^{\frac{n-1}{2}} \tag{31}$$

Here $\dot{\varepsilon}_{xx}$, $\dot{\varepsilon}_{yy}$, $\dot{\varepsilon}_{xy}$ and $\dot{\varepsilon}_{xz}$ are strain rates associated with longitudinal extension, lateral compression, side drag, and basal drag, respectively. Lateral compression occurs when slow sheet flow converges on fast stream flow, but ice streams have relatively constant widths. There is no lateral shear down the centerline of ice streams, and there is little basal shear if the bed is wet and φ is high. So $\dot{\varepsilon}_{xx}$ is the dominant strain rate and $R \approx 1$ for $n = 3$ is a useful approximation. However, $\dot{\varepsilon}_{xy}$ cannot be ignored for narrow ice streams (Dupont and Alley, 2005a, b). For the central flowline of a narrow ice stream, the contribution from $\dot{\varepsilon}_{xy}$ can be added to $\dot{\varepsilon}_{xz}$.

Collecting terms in Eq. (20):

$$(1 - 2\varphi + 2\varphi^2)\Delta h/\Delta x = \varphi^2\left(\frac{\Delta h}{\Delta x}\right)_F + (1-\varphi)^2\left(\frac{\Delta h}{\Delta x}\right)_G \tag{32}$$

Writing as a quadratic equation:

$$\left[2\left(\frac{\Delta h}{\Delta x}\right) - \left(\frac{\Delta h}{\Delta x}\right)_F - \left(\frac{\Delta h}{\Delta x}\right)_G\right]\varphi^2 - \left[2\left(\frac{\Delta h}{\Delta x}\right) - 2\left(\frac{\Delta h}{\Delta x}\right)_G\right]\varphi \tag{33}$$

$$+\left[\left(\frac{\Delta h}{\Delta x}\right)-\left(\frac{\Delta h}{\Delta x}\right)_{\mathrm{G}}\right]=0$$

Setting $C_1 = (\Delta h/\Delta x)$, $C_2 = (\Delta h/\Delta x)_{\mathrm{F}}$, and $C_3 = (\Delta h/\Delta x)_{\mathrm{G}}$ and solving for φ gives the solution for an ice stream having constant width and side shear:

$$\varphi = \frac{(C_1 - C_3) \pm \left[(C_1 - C_3)^2 - (C_1 - C_3)(2C_1 - C_2 - C_3)\right]^{\frac{1}{2}}}{(2C_1 - C_2 - C_3)} \tag{34}$$

In a flowline solution, width $w_{\mathrm{I}} = 0$ so $\tau_{\mathrm{S}} = 0$. Yet side drag remains and contributes to the ice elevation needed to overcome resistance to ice flow, so it must be taken into account in some way, especially for narrow ice streams (Dupont and Alley, 2005a, b). The best way is to enlarge τ_{O} to effective basal shear stress τ_{O}^* linked to areas $5+6$ minus areas $1+2$ as incremental length $\Delta x \rightarrow 0$ in Fig. 5. Then τ_{O}^* is:

$$\tau_{\mathrm{O}}^* = \rho_{\mathrm{I}} g h_{\mathrm{I}} (1-\varphi^2)\Delta h/\Delta x - \rho_{\mathrm{I}} g h_{\mathrm{I}}^2 \varphi \Delta\varphi/\Delta x \tag{35}$$

and the longitudinal force balance, putting the $\Delta\varphi/\Delta x$ terms in Eqs. (16) through (18) between Δx steps, becomes (Hughes, 2012, Chapter 11):

$$\frac{\Delta h}{\Delta x} = \frac{\Delta(\rho_{\mathrm{F}} h_{\mathrm{I}})/\Delta x}{P_{\mathrm{I}}} + \frac{\tau_{\mathrm{O}}^*}{P_{\mathrm{I}}} = \varphi^2 \left(\frac{\Delta h}{\Delta x}\right)_{\mathrm{F}} + (1-\varphi^2)\left(\frac{\Delta h}{\Delta x}\right)_{\mathrm{G}} \tag{36}$$

Collecting terms containing φ gives:

$$\left[\left(\frac{\Delta h}{\Delta x_{\mathrm{G}}}\right)-\left(\frac{\Delta h}{\Delta x_{\mathrm{F}}}\right)\right]\varphi^2 - \left[\left(\frac{\Delta h}{\Delta x_{\mathrm{G}}}\right)-\left(\frac{\Delta h}{\Delta x}\right)\right] = 0 \tag{37}$$

Solving for φ gives the solution for an ice-stream centerline with side shear added to basal shear:

$$\varphi = \pm\left[\frac{C_3 - C_1}{C_3 - C_2}\right]^{\frac{1}{2}} \tag{38}$$

cc BY

In Eqs. (34) and (38), the correct solution puts φ in the range $0 \le \varphi \le 1$.

Equation (33) includes $(\Delta h/\Delta x)_F$ for floating fraction φ of ice in our model, linked to longitudinal strain rate $\dot{\varepsilon}_{xx}$ as seen in Eq. (29), and also to the flow law of ice given by Eq. (30) which links $\dot{\varepsilon} = \dot{\varepsilon}_{xz}$ to σ_T given by Eq. (12). The longitudinal strain rate is therefore, using Eq. (12) for σ_T and following Hughes (2012, Chapter 12):

$$\begin{aligned}\dot{\varepsilon} = \dot{\varepsilon}_{xx} = (\sigma_T/2A)^n &= \left[(\rho_I g h_I/4A)(1-\rho_I/\rho_W)\varphi^2\right]^n \\ &= \left[(\rho_I g h_I/4A)(1-\rho_I/\rho_W) - (\sigma_B/2A)\right]^n\end{aligned} \tag{39}$$

Here σ_B is a back-stress due to buttressing by a confined and pinned ice shelf given by:

$$\sigma_B = f_B\left[\frac{1}{2}\rho_I g h_O(1-\rho_I/\rho_W)\right] \tag{40}$$

where f_B is a buttressing fraction with $f_B = 0$ for no buttressing and $f_B = 1$ for full buttressing.

Equations (34) and (38) allow two treatments for $\dot{\varepsilon}$ varying along x in these equations. One treatment uses Eq. (39) to emphasize φ at $x > 0$:

$$\dot{\varepsilon} = \left[(\rho_I g h_I/4A)(1-\rho_I/\rho_W)\varphi^2\right]^n \tag{41}$$

with $\varphi^2 = [1 - f_B(h_O/h_I)]$ at $x = 0$ being a measure of ice-shelf buttressing such that $\varphi = 1$ if the ice shelf has disintegrated so $f_B = 0$. If φ is replaced by ice-shelf buttressing at $x = 0$, then Eq. (39) gives the other treatment with Eq. (40) substituted for σ_B to emphasize f_B for buttressing at $x = 0$:

$$\dot{\varepsilon} = \left[(\rho_I g h_I/4A)(1-\rho_I/\rho_W)\right]^n\left[1 - f_B(h_O/h_I)\right]^n \tag{42}$$

TCD
8, 2043–2118, 2014

CC BY

Equation (42) shows that ice-shelf buttressing, like φ, is transmitted upstream. With either Eq. (41) or Eq. (42) substituted for $\dot{\varepsilon}$ in Eq. (29), we see that $(\Delta h/\Delta x)_F$ varies with either φ^6 or $[1 - f_B(h_O/h_I)]^3$ for $n = 3$. Both possibilities will be considered. In the case of Eq. (42), $0 \le f_B \le 1$ is chosen to conform with the observed h_O at the ice-shelf grounding line, since unbuttressing decreases h_O over time due to enhanced ice-shelf thinning. When the ice shelf has disintegrated, $f_B = 0$ is expected. Equation (42) should be compared with one used by Thomas (2004) in modeling the ongoing surge of Jakobshavn Isbrae following disintegration of its buttressing ice shelf in Jakobshavn Isfjord.

4 Ice-bed uncoupling for shelf flow

The ability of ice shelves to buttress ice streams was recognized early (Hughes, 1972, 1973; Thomas, 1973a, b), but has only recently gained wide acceptance and spurred efforts at holistic ice sheet modeling, see Thomas (2004), Thomas et al. (2004), Dupont and Alley (2005, 2006), and Gagliardini et al. (2010) for numerical models, Schoof (2007) for a theoretical model, and Rignot et al. (2004), Scambos et al. (2004), and Pritchard et al. (2009) for field studies. One reason for the hesitation is illustrated in Fig. 5. Shear resistance to ice flow is represented by the shaded part of the longitudinal gravitational driving force given by triangular area $\overline{P}_I h_I$ per unit flowband width w_I. This shaded area vanishes when ice becomes afloat, leaving only water triangle 1 having area $\overline{P}_W h_W$ as the longitudinal force of water buttressing the ice. This is the case whether or not an ice shelf exists, so that $\varphi = 1$ at $x = 0$. However, side shear can exist for an ice shelf in a confining embayment, even if flowbands from ice streams that supply the ice shelf move with the velocity of shelf flow, so these flowbands have little or no side shear, as is generally observed for the large Antarctic ice shelves that buttress ice streams.

CC BY

As in Thomas (2004), compressive stress σ_C at x results from all downstream resistance to ice flow. A longitudinal force balance for constant w_I gives, referring to Fig. 5 (top):

$$\sigma_C A_x = \sigma_C h_I w_I = \overline{\tau_O}(w_I x + A_R) + \overline{\tau_S}\left(2\overline{h_I}x + 2\overline{h_S}L_S + \overline{h_R}C_R\right) + \left(\overline{P_W}h_W\right)_O w_I \quad (43)$$

where $\overline{\tau_O}$ is the average basal shear stress over downslope basal area $w_I x$ of the ice stream and basal area A_R of ice rumples on the ice shelf, $\overline{\tau_S}$ is the average side shear stress over downslope side areas $2\overline{h_I}x$ of the ice stream, $2\overline{h_S}L_S$ of the ice shelf, and $\overline{h_R}C_R$ of ice rises on the ice shelf for average ice thickness $\overline{h_I}$ along length x of the ice stream, $\overline{h_S}$ along grounded side lengths L_S of the ice shelf, and $\overline{h_R}$ around circumference C_R of ice rises, and $\left(\overline{P_W}h_W\right)_O w_I$ is the back-force at $x = 0$ due to average water pressure $\overline{P_W}$ in water of depth h_W at the ice-shelf grounding line. For ice rumples and ice rises with mean ice thickness $\overline{h_D}$ in transverse diameter $\overline{D_R}$, the local respective compressive stresses on the stoss side are $\sigma_D = \left(A_R/D_R\overline{h_D}\right)\tau_O$ and $\sigma_D = \left(C_R\overline{h_R}/D_R\overline{h_D}\right)\tau_S$, where σ_D adds to σ_C. In Eq. (43), therefore, compressive force $\sigma_C A_x$ at x on the left side is the result of average downslope basal and side shear forces and a water-pressure force at $x = 0$, all on the right side. Solving for σ_C:

$$\sigma_C = \frac{\overline{\tau_O}(w_I x + A_R) + \overline{\tau_S}\left(2\overline{h_I}x + 2\overline{h_S}L_S + \overline{h_R}C_R\right) + \left(\overline{P_W}h_W\right)_O w_I}{h_I w_I} \quad (44)$$

Gravitational force $(F_G)_1$ at x is w_I times the area of triangle 1 in Fig. 5 (bottom). It is resisted by a downslope basal shear force $(F_O)_1$ given by mean downslope basal shear stress $\overline{\tau_O}$ times basal area $w_I x$ beneath the ice stream and total area A_R beneath ice rumples on the ice shelf. Since triangle 1 occupies the shaded area in Fig. 5 (top), its basal ice pressure $(P_I)_1 = \rho_I g(h_I - h_F)$ is supported by the bed and its mean downstream

CC BY

ice pressure $\left(\overline{P_{\mathrm{I}}}\right)_1 = 1/2(P_{\mathrm{I}})_1$ is exerted over area w_{I} times triangle height $h_{\mathrm{I}} - h_{\mathrm{F}}$. Equating this negative gravitational force $(F_{\mathrm{G}})_1 = \left(\overline{P_{\mathrm{I}}}\right)_1 (h_{\mathrm{I}} - h_{\mathrm{F}})w_{\mathrm{I}} = 1/2\rho_{\mathrm{I}} g (h_{\mathrm{I}} - h_{\mathrm{F}})^2 w_{\mathrm{I}}$ with positive down-stream resisting force $(F_{\mathrm{O}})_1 = \overline{\tau_{\mathrm{O}}}(w_{\mathrm{I}} x + A_{\mathrm{R}})$ and solving for $\overline{\tau_{\mathrm{O}}}$ using $h_{\mathrm{F}} = h_{\mathrm{I}}\varphi$ gives:

$$\overline{\tau_{\mathrm{O}}} = \frac{1/2\rho_{\mathrm{I}} g (h_{\mathrm{I}} - h_{\mathrm{F}})^2 w_{\mathrm{I}}}{w_{\mathrm{I}} x + A_{\mathrm{R}}} = \frac{1/2\rho_{\mathrm{I}} g h_{\mathrm{I}} (1-\varphi)^2 h_{\mathrm{I}} w_{\mathrm{I}}}{w_{\mathrm{I}} x + A_{\mathrm{R}}} = \frac{\overline{P_{\mathrm{I}}}(1-\varphi)^2 h_{\mathrm{I}} w_{\mathrm{I}}}{w_{\mathrm{I}} x + A_{\mathrm{R}}} \tag{45}$$

Triangular areas 1, 3, and 4 in Fig. 5 (bottom) have now been linked to $\overline{P_{\mathrm{I}}}$ and φ through stresses $\overline{\tau_{\mathrm{O}}}$, σ_{W}, and σ_{T}, respectively. All that remains is the area of rectangle 2 in Fig. 5 (bottom) and $\overline{\tau_{\mathrm{S}}}$ for side shear averaged over downslope side areas $2\,\overline{h_{\mathrm{I}}}x$ of the ice stream and side areas $2\,\overline{h_{\mathrm{S}}}L_{\mathrm{S}}$ and $\overline{h_{\mathrm{R}}}C_{\mathrm{R}}$ of the ice shelf and ice rises having total grounded side lengths $2L_{\mathrm{S}}$ and circumference C_{R}, respectively, as shown in Fig. 5 (top). The negative downstream gravitational force given by w_{I} times the area of rectangle 2 for $(P_{\mathrm{I}})_1 = (P_{\mathrm{I}})_2$ is $(F_{\mathrm{G}})_2 = (P_{\mathrm{I}})_2 h_{\mathrm{F}} w_{\mathrm{I}} = \rho_{\mathrm{I}} g (h_{\mathrm{I}} - h_{\mathrm{F}}) h_{\mathrm{F}} w_{\mathrm{I}}$. It is resisted by positive downstream side shear force $(F_{\mathrm{S}})_2 = \overline{\tau_{\mathrm{S}}}(2\overline{h_{\mathrm{I}}}x + 2\overline{h_{\mathrm{S}}}L_{\mathrm{S}} + \overline{h_{\mathrm{R}}}C_{\mathrm{R}})$. Equating these forces and solving for τ_{S} using $h_{\mathrm{F}} = h_{\mathrm{I}}\varphi$ gives:

$$\overline{\tau_{\mathrm{S}}} = \frac{\rho_{\mathrm{I}} g (h_{\mathrm{I}} - h_{\mathrm{F}}) h_{\mathrm{F}} w_{\mathrm{I}}}{2\overline{h_{\mathrm{I}}}x + 2\overline{h_{\mathrm{S}}}L_{\mathrm{S}} + \overline{h_{\mathrm{R}}}C_{\mathrm{R}}} = \frac{\rho_{\mathrm{I}} g h_{\mathrm{I}} (1-\varphi)\varphi h_{\mathrm{F}} w_{\mathrm{I}}}{2\overline{h_{\mathrm{I}}}x + 2\overline{h_{\mathrm{S}}}L_{\mathrm{S}} + \overline{h_{\mathrm{R}}}C_{\mathrm{R}}} = \frac{P_{\mathrm{I}}(1-\varphi)\varphi h_{\mathrm{F}} w_{\mathrm{I}}}{2\overline{h_{\mathrm{I}}}x + 2\overline{h_{\mathrm{S}}}L_{\mathrm{S}} + \overline{h_{\mathrm{R}}}C_{\mathrm{R}}} \tag{46}$$

Equation (11) can now be solved for φ using Eqs. (12) and (13) for σ_{T} and σ_{C}, respectively. First, substitute Eqs. (45) and (46) for $\overline{\tau_{\mathrm{O}}}$ and $\overline{\tau_{\mathrm{S}}}$ in Eq. (44):

$$\sigma_{\mathrm{C}} = \frac{\left(\overline{P_{\mathrm{W}}}h_{\mathrm{W}}\right)_{\mathrm{O}}}{h_{\mathrm{I}}} + \left[\frac{\overline{P_{\mathrm{I}}}(1-\varphi)^2}{w_{\mathrm{I}} x + A_{\mathrm{R}}}\right](w_{\mathrm{I}} x + A_{\mathrm{R}}) + \left[\frac{P_{\mathrm{I}}(1-\varphi)\varphi}{2\overline{h_{\mathrm{I}}}x + 2\overline{h_{\mathrm{S}}}L_{\mathrm{S}} + \overline{h_{\mathrm{R}}}C_{\mathrm{R}}}\right]\left(2\overline{h_{\mathrm{I}}}x + 2\overline{h_{\mathrm{S}}}L_{\mathrm{S}} + \overline{h_{\mathrm{R}}}C_{\mathrm{R}}\right) \tag{47}$$

TCD
8, 2043–2118, 2014

cc BY

$$=\frac{1}{2}\rho_I g\left(h_O^2/h_I\right)(\rho_I/\rho_W)+\frac{1}{2}\rho_I g h_I(1-\varphi)^2+\rho_I g h_I(1-\varphi)\varphi$$
$$=\frac{1}{2}\rho_I g h_O(\rho_I/\rho_W)(h_O/h_I)+\frac{1}{2}\rho_I g h_I(1-2\varphi+\varphi^2+2\varphi-2\varphi^2)$$
$$=\frac{1}{2}\rho_I g h_I(\rho_I/\rho_W)(h_O/h_I)+\frac{1}{2}\rho_I g h_I(1-\varphi^2)$$

Combining Eqs. (13) and (47) leads to Eq. (21), see Hughes (1012, Chapter 11).

Ice elevation h a.s.l. at the ice-shelf grounding line is given by the buoyancy requirement $h = h_O(1-\rho_I/\rho_W)$ for respective ice and water densities ρ_I and ρ_W. At the grounding line, horizontal force $1/2P_O h_O$ in ice minus horizontal force $1/2P_W h_W$ in water is balanced by longitudinal tensile force $\sigma_T h_O$, where $P_O = \rho_I g h_O = P_W = \rho_W g h_W$ are the respective ice and water pressures at the base where $h_W < h_O$ is water depth below sea level. Balancing these forces gives:

$$\sigma_T = 1/2\rho_I g h_O(1-\rho_I/\rho_W) \tag{48}$$

The closest approximation to keeping $h_I = h_O$ everywhere on the ice shelf occurs if the ice shelf occupies a confining embayment and ice is locally pinned to the bed so ice rises (strong pinning) and ice rumples (weak pinning) develop on the ice surface. Then back-stress σ_B buttresses the ice stream at the ice-shelf grounding line, where σ_B is subtracted from σ_T given by Eq. (48):

$$\sigma_T = 1/2\rho_I g h_O(1-\rho_I/\rho_W)-\sigma_B \tag{49}$$

With this subtraction, solving Eq. (49) for h_O gives:

$$h_O = 2(\sigma_T+\sigma_B)/\rho_I g(1-\rho_I/\rho_W) \tag{50}$$

Equation (50) shows that h_O increases as σ_B increases due to ice-shelf confinement and pinning, with σ_B given by Eq. (40).

cc BY

Ice-shelf buttressing of ice streams was included in the derivation of Eq. (40), so ice thickness h_O at their (un)grounding lines includes the additional ice thickness when an ice shelf is grounded laterally and locally. To quantify buttressing, an unbuttressing factor φ_O at $x = 0$ is needed for ice shelves such that $\varphi_O = 1$ for freely floating ice beyond the grounding line (no buttressing) and $\varphi_O = 0$ when the entire ice shelf is fully enclosed or fully grounded (full buttressing).

Ice-shelf buttressing can be quantified by applying Eq. (12) to the ice-shelf grounding line, where $x = 0$, $h_I = h_O$, and $\varphi = 1$ gives $h_W/h_O = \rho_I/\rho_W$, and $(\sigma_C)_O$ is given by Eq. (44) at $x = 0$. Then $(\overline{P}_I)_O = (\overline{P}_W)_O$ and:

$$
\begin{aligned}
(\sigma_T)_O &= \left(\overline{P}_I - \sigma_C\right)_O = \left(\overline{P}_I\right)_O - \left[\overline{\tau_O} A_R + \overline{\tau_S}\left(2\overline{h}_S L_S + \overline{h}_R C_R\right) + \left(\overline{P}_W h_W\right)_O w_I\right] / h_O w_I \qquad (51)\\
&= \left[\overline{P}_I - \overline{P}_W(\rho_I/\rho_W)\right]_O - \left[\overline{\tau_O} A_R + \overline{\tau_S}\left(2\overline{h}_S L_S + \overline{h}_R C_R\right)\right] / h_O w_I \\
&= \left(\overline{P}_I\right)_O (1 - \rho_I/\rho_W) - (\sigma_B)_O
\end{aligned}
$$

Comparing Eq. (51) with Eq. (12) for $\varphi = 1$ at $x = 0$ shows that compressive stress $(\sigma_B)_O$ is a result of ice-shelf buttressing, as formulated by Thomas (1973a, b):

$$
(\sigma_B)_O = \left[\overline{\tau_O} A_R + \overline{\tau_S}\left(2\overline{h}_S L_S + \overline{h}_R C_R\right)\right] / h_O w_I \qquad (52)
$$

where $(\sigma_B)_O = 0$ in the absence of a confining embayment and basal pinning points that impede pure shelf flow. Figure 7 represents an ice shelf that buttresses an ice stream. The ice shelf is confined in an embayment and pinned at ice rumples and ice rises. Ice shears over pinning points causing ice rumples and shears around pinning points causing ice rises.

CC BY

Define an ice-shelf buttressing factor φ_O at $x = 0$ in terms of partial ice-shelf grounding at its base and along its perimeter as follows:

$$\varphi_O = 1 - \left[\frac{\psi A_R}{A_F + A_R} + \frac{(1-\psi)\left(L_G\overline{h_G} + C_R\overline{h_R}\right)}{L_F\overline{h_F} + L_G\overline{h_G} + C_R\overline{h_R}} \right] \tag{53}$$

Here A_R is the grounded area of ice rumples, A_F is the floating area, $L_G\overline{h_G}$ is the area of side grounding of length L_G and mean ice thickness $\overline{h_G}$, $C_R\overline{h_R}$ is the perimeter area of ice rises of circumference C_R and mean ice thickness $\overline{h_R}$, and $L_F\overline{h_F}$ is the floating area along the calving front of length L_F and mean ice thickness $\overline{h_F}$. The force ratio of grounded areas exposed to mean basal shear stress $\overline{\tau_O}$ to grounded areas exposed to both $\overline{\tau_O}$ and to mean side shear stress $\overline{\tau_S}$ is fraction ψ defined as:

$$\psi = \frac{A_R\overline{\tau_O}}{A_R\overline{\tau_O} + \left(L_G\overline{h_G} + C_R\overline{h_R}\right)\overline{\tau_S}} \approx \frac{A_R}{A_R + 2\left(L_G\overline{h_G} + C_R\overline{h_R}\right)} \tag{54}$$

where $\overline{\tau_S} \approx 2\overline{\tau_O}$ because each of these shear stresses is close to one of the two viscoplastic yield stresses σ_V of ice in Fig. 2. Temperate basal ice slides across pinning points to produce ice rumples on the surface, so $\sigma_V = 38.6\,\mathrm{kPa}$ can be used, whereas cold ice shearing around pinning points that penetrate basal ice to produce ice rises on the surface probably requires $\sigma_V = 66.7\,\mathrm{kPa}$, assuming yielding in cold ice requires heat produced by strain rate $\dot{\varepsilon}_O$ as already discussed.

Equation (53) gives $\varphi_O = 0$ when $A_F = L_F = 0$ and $\psi = 1$ for an ice stream ending as an ice lobe grounded on land or when $A_R = L_F = C_R = 0$ and $\psi = 0$ for a fully enclosed ice shelf, and $\varphi_O = 1$ when $A_R = L_G = C_R = 0$ for an ice stream ending as a freely floating ice shelf. Then $0 < \varphi_O < 1$ specifies the degree of ice-shelf grounding; that is, of ice-bed coupling responsible for ice-shelf buttressing. Equation (51) may now be written:

$$(\sigma_\text{T})_\text{O} = \left(\overline{P_\text{I}}\right)_\text{O}(1-\rho_\text{I}/\rho_\text{W}) - (\sigma_\text{B})_\text{O} = \left(\overline{P_\text{I}}\right)_\text{O}(1-\rho_\text{I}/\rho_\text{W})\varphi_\text{O} = (\sigma_\text{U})_\text{O}\varphi_\text{O} \tag{55}$$

where $(\sigma_\text{U})_\text{O} = \left(\overline{P_\text{I}}\right)_\text{O}$ (1 - $\rho_\text{I}/\rho_\text{W}$) is σ_T at $h_\text{I} = h_\text{O}$ in Eq. (44) for an unconfined ice shelf that provides no buttressing from grounding. Solving Eq. (55) for φ_O:

$$\varphi_\text{O} = \frac{\left(\overline{P_\text{I}}\right)_\text{O}(1-\rho_\text{I}/\rho_\text{W}) - (\sigma_\text{U})_\text{O}}{\left(\overline{P_\text{I}}\right)_\text{O}(1-\rho_\text{I}/\rho_\text{W})} = \frac{(\sigma_\text{U})_\text{O} - (\sigma_\text{B})_\text{O}}{(\sigma_\text{B})_\text{O}} = 1 - \left(\frac{\sigma_\text{B}}{\sigma_\text{U}}\right)_\text{O} \tag{56}$$

Eliminate φ_O by equating Eqs. (53) and (56):

$$\left(\frac{\sigma_\text{B}}{\sigma_\text{U}}\right)_\text{O} = \frac{\psi A_\text{R}}{A_\text{F} + A_\text{R}} + \frac{(1-\psi)\left(L_\text{G}\overline{h_\text{G}} + C_\text{R}\overline{h_\text{R}}\right)}{L_\text{F}\overline{h_\text{F}} + L_\text{G}\overline{h_\text{G}} + C_\text{R}\overline{h_\text{R}}} \tag{57}$$

Equation (57) gives $\sigma_\text{B} = 0$ when $A_\text{R} = L_\text{G} = C_\text{R} = 0$ and $\sigma_\text{B} = \sigma_\text{U}$ when $A_\text{F} = L_\text{F} = 0$ for $0 \le \psi \le 1$. The ice stream ends as a fully grounded ice lobe when $A_\text{F} = 0$ and $\psi = 1$, and ends as a fully enclosed ice shelf when $A_\text{R} = L_\text{F} = C_\text{R} = 0$ and $\psi = 0$. In these cases $\sigma_\text{B} = \sigma_\text{U}$ for full buttressing, with $(\sigma_\text{T})_\text{O} = 0$ in Eq. (55) for $\varphi_\text{O} = 0$.

Equation (56) preserves in φ_O the definition of φ as a floating fraction. It also suggests a basal buoyancy factor φ_B defined as:

$$\varphi_\text{B} = \varphi\varphi_\text{O} \tag{58}$$

where φ represents the loss of ice-bed coupling under an ice stream as φ increases, and φ_O represents the loss of ice-shelf buttressing beyond the ice stream as φ_O increases (Hughes, 1992, 2011, 2012, Chapter 25).

A terrestrial ice stream commonly ends as a terminal ice lobe grounded on land. Ice lobes are typically thin because of weak ice-bed coupling due to high basal water pressure that supersaturates and mobilizes subglacial till. However, this water drains away around the ice-lobe perimeter so the buoyancy requirement is lost even though the bed remains wet and soft. If h_O is ice height above the bed at distance x from the lobe margin given by Eq. (1), let basal drag provide resistance comparable to grounding due to confinement and pinning of an ice shelf so $\tau_O x = h_O \sigma_B$ to a first approximation, with buoyancy no longer satisfied so $\sigma_T = 1/2 \rho_I g h_O$. Then Eq. (1) gives for longitudinal force balance $\sigma_T h_O - \sigma_B h_O = 0$:

$$\sigma_T = \sigma_B = 1/2 \rho_I g h_O = 1/2 P_O = \overline{P_O} \tag{59}$$

That h_O is small when ice streams end as ice lobes on land has been shown from glacial geology and modeling studies for southern lobes of the former Laurentide Ice Sheet (Clark, 1992; Jenson et al., 1995, 1996; Carlson et al., 2007). This is because σ_T and σ_B are essentially equal in magnitude. An ice lobe is not so different from an ice shelf when area A_R for ice rumples is the total basal area of the ice lobe, so $A_F = 0$ and $\psi = 1$ in Eq. (53). However, Eq. (50) shows that h_O can be quite large for ice streams buttressed by floating ice shelves, up to1000 m or more for ice shelves occupying confining embayments and locally pinned to the sea floor, producing ice rumples and ice rises on the surface, respectively where ice scrapes across weaker pinning points and flows around stronger pinning points.

Table 1 links Eq. (58) to the life cycle of an ice stream, beginning with $\varphi_B = \varphi = \varphi_O = 1$ and ending with $\varphi_B = \varphi = \varphi_O = 0$. Note that an ice stream shuts down when either φ or φ_O is zero, leaving only slow sheet flow. The point here is that ice-bed coupling is quantified by floating fraction φ at $x > 0$ linked to longitudinal and shear stresses that resist stream flow, whereas ice-shelf buttressing is quantified by φ_O at $x = 0$ linked to grounding ranging from a freely floating ice tongue to a fully confined ice shelf or a fully grounded ice lobe, without invoking resisting stresses. Their product φ_B then quantifies coupling for sheet, stream, and shelf flow. Any path can be taken between $\varphi_B = 1$ and $\varphi_B = 0$, as well as paths that remain between these limits so no life cycle is completed. Two paths are worth mention and are examined next. One moves along the

cc BY

φ axis and represents increasing ice-bed coupling, called here the Zwally Effect (Zwally et al., 2002) The other moves along the φ_O axis and represents increasing ice-shelf buttressing, called here the Thomas Effect (Thomas, 2004). Their studies were made near and on Jakobshavn Isbrae, respectively. Movement along both axes quantifies the Jakobshavn Effect by $\varphi_B = \varphi\varphi_O$. Table 1 replaces the similar table in Hughes (1992).

In Eqs. (34) and (38), from Eqs. (29), (30), and (12):

$$C_2 = \left(\frac{\Delta h}{\Delta x}\right)_F = \frac{h_I(a-r) - h_I^2\dot{\varepsilon}}{h_O u_O + (a-r)x} - \frac{h_I(a-r) - h_I^2 R(\sigma_T/2A)^n}{h_O u_O + (a-r)x} \tag{60}$$

$$= \frac{h_I(a-r)}{h_O u_O + (a-r)x} - \frac{h_I^2 R}{h_O u_O + (a-r)x}\left[\frac{\rho_I g h_I (1-\rho_I/\rho_W)\varphi^2}{4A}\right]^n$$

For ice-shelf buttressing at $x = 0$ where $h_I = h_O$ and $\varphi = \varphi_O$, Eq. (56) gives $\varphi_O = (1 - \sigma_B/\sigma_U)_O = 1 - f_B(h_O/h_I)$ from Eqs. (38) and (40). With these changes:

$$C_2 = \frac{h_I(a-r)}{h_O u_O + (a-r)x} - \frac{h_I^2 R}{h_O u_O + (a-r)x}\left[\frac{\rho_I g h_I (1-\rho_I/\rho_W)}{4A}\left(1 - \frac{\sigma_B}{\sigma_U}\right)_O^2\right]^n \tag{61}$$

$$= \frac{h_I(a-r)}{h_O u_O + (a-r)x} - \frac{h_I^2 R}{h_O u_O + (a-r)x}\left[\frac{\rho_I g h_I (1-\rho_I/\rho_W)}{4A}\right]^n \left[1 - f_B\left(\frac{h_O}{h_I}\right)\right]^{2n}$$

For full ice-shelf buttressing, $f_B = 1$ and:

$$C_2 = \frac{h_I(a-r)}{h_O u_O + (a-r)x} - \frac{h_I^2 R}{h_O u_O + (a-r)x}\left[\frac{\rho_I g h_I (1-\rho_I/\rho_W)}{4A}\right]^n \left[1 - \frac{h_O}{h_I}\right]^{2n} \tag{62}$$

For no ice-shelf buttressing, $f_B = 0$ and:

$$C_2 = \frac{h_I(a-r)}{h_O u_O + (a-r)x} - \frac{h_I^2 R}{h_O u_O + (a-r)x}\left[\frac{\rho_I g h_I (1-\rho_I/\rho_W)}{4A}\right]^n \tag{63}$$

Note that h_O/h_I is φ using only the force balance, see Eq. (21).

TCD
8, 2043–2118, 2014

CC BY

5 Ice-bed uncoupling for Byrd Glacier

In the Jakobshavn Effect, ice-bed uncoupling under ice streams is caused by summer surface meltwater that reaches the bed through crevasses and moulins. Very little summer surface melting occurs on Byrd Glacier, and none reaches the bed. So as a proxy for ice-bed uncoupling by this mechanism, we used the rapid discharge from two subglacial lakes in the zone of strongly converging flow just above Byrd Glacier reported by Stearns et al. (2008).

Figure 8 is a satellite image of Byrd Glacier showing the centerline along which floating fraction φ is calculated. Figure 9 shows profiles of the ice surface, base, and thickness along the centerline, and the location of the (un)grounding line. Byrd Glacier occupies a fjord through the Transantarctic Mountains called Barne Inlet, it has the largest ice catchment/drainage basin of any Antarctic ice stream, and it supplies the Ross Ice Shelf with more ice than any other ice stream. It becomes ungrounded in the fjord and moves much faster than the ice shelf, so giant rifts separate it from the ice shelf for some 40 km beyond the fjord until the rifts heal and the Byrd Glacier flowband moves with the same velocity as the ice shelf. Initial surface velocities on Byrd Glacier were made by Swithinbank (1963) across the floating portion. Surface velocities and elevations were measured photogrammetrically over the whole surface by Brecher (1982). The Center for Remote Sensing of Ice Sheets (CReSIS) conducted a comprehensive radar-mapping survey of surface and bed topography in the map plane, see Fig. 10. In recent years, subglacial lakes were found to be ubiquitous under the Antarctic Ice Sheet, and were often interconnected, allowing ice tributaries to form and supply major ice streams that discharge about 90 % of Antarctic ice (Rignot et al., 2011). Two such lakes, shown in Fig. 10, were located about 200 km inland from Barne Inlet. The peak water discharge from late 2006 to early 2007 was measured by lowered ICESat surface elevations, and coincided with a ten percent increase in velocity of Byrd Glacier along its whole length, jumping to 900 m a^{-1} where Byrd Glacier became afloat in Barne Inlet

(Stearns et al., 2008). Since then the lakes have been refilling. This mechanism for ice-bed uncoupling substitutes for surface water reaching the bed.

Lake-drainage coincident with velocity increases can be linked to reductions in ice-bed coupling under Byrd Glacier caused by an increase in floating fraction φ of ice when lake water flooded through Barne Inlet to the Ross Sea under the Ross Ice Shelf. Increases in φ can be calculated from Eq. (34) using width w_I of Byrd Glacier when side shear along the fjord walls is included, and from Eq. (38) along the centerline of Byrd Glacier where side shear is absent. Data used to evaluate C_1 are measured ice surface slopes $\Delta h/\Delta x$ in incremental distances Δx along x, with $x = 0$ where Byrd Glacier becomes afloat about 25 km from the entrance to Barne Inlet. Evaluations of C_2 for $(\Delta h/\Delta x)_F$ use estimated values of $(a - r) = 23 \times 10^{-3}\,\mathrm{m\,a^{-1}}$ averaged along x (Hughes et al., 2011), and measured values of h_O where ice becomes afloat, $x = 0$ in Eqs. (34) and (38), and $\dot{\varepsilon}_{xx}$ along x in 1978–1979 (Whillans et al., 1989), see Eq. (29). Alternatively, $\dot{\varepsilon}_{xx}$ can be calculated using the φ dependence of $\dot{\varepsilon}_{xx}$ in Eq. (39), taking $\rho_I = 917\,\mathrm{kg\,m^{-3}}$, $\rho_W = 1000\,\mathrm{kg\,m^{-3}}$, $g = 9.81\,\mathrm{m\,s^{-1}}$, $A = 250\,\mathrm{MPa\,s^{1/3}} = 7.9\,\mathrm{bar\,a^{1/3}} \approx 8\,\mathrm{bar\,a^{1/3}}$, $n = 3$, and measured values of h_I along x in Fig. 9 (Hughes et al., 2011), with $\sigma_B = 1/2\rho_I g h_O(1 - \rho_I/\rho_W)$ for $\varphi = 1$ at $x = 0$ for full buttressing by the Ross Ice Shelf. Then $\dot{\varepsilon}_{xx} = 0$ at $x = 0$ as observed (Brecher, 1982; Whillans et al., 1989). We used this alternative approach. Evaluations of C_3 for $(\Delta h/\Delta x)_G$ use $B = 1.123 \times 10^4\,\mathrm{kPa\,s^{1/2}\,m^{-1/2}} = 0.02\,\mathrm{bar\,a^{1/2}\,m^{-1/2}}$, $m = 2$, $L = 1250\,\mathrm{km}$, $h_O = 1.3\,\mathrm{km}$ at $x = 0$, and measured values of h_I along x (Hughes et al., 2011), see Eq. (26) with h_I measured along x for Byrd Glacier.

Figure 10 plots φ along x using Eq. (34) for width $w_I = 25\,\mathrm{km}$ across Byrd Glacier with side shear along the fjord walls, using Eq. (38) for the centerline of Byrd Glacier with side shear incorporated into basal shear, both equations combining the force balance with the mass balance, and also using Eq. (21) obtained from the force balance only. Values of φ using $A = 8.0\,\mathrm{bar\,a^{1/3}}$ drop rapidly to 0.10 from hovering around 0.80 with side shear and around 0.95 with side shear incorporated into basal shear, Eqs. (34)

and (38) respectively, both at about 50 km from $x = 0$ at the beginning of the radar profile. This is the shortest distance where floating ice may have become grounded. From there on, $\varphi = 0.10 \pm 0.05$ for mostly grounded ice.

A floating-ice requirement at the beginning of the radar profile can be enforced by setting $\varphi = 1.0$ at $x = 0$ and solving for ice hardness parameter A in Eqs. (34) and (38). Then $A = 23\,\mathrm{bar\,a}^{1/3}$ and floating ice grounds about 90 km from $x = 0$, see Fig. 9. Ice elevation then increases all the way up Byrd Glacier, as is expected for increasing ice-bed coupling. This is reflected in $\varphi = 0.15 \pm 0.5$ under most of Byrd Glacier. In all cases, $\varphi \rightarrow 0$ at a bedrock low point about halfway up the fjord ($x \approx 150$ km). Variations in φ have no obvious correlation with bed topography, but peaks in φ have some correlation with more gentle surface slopes, which is compatible with reduced ice-bed coupling. Values of φ were smoothed using the Benzier method, since φ is sensitive to variations in surface slopes not directly related to ice-bed coupling, such as ablation rates related to variations in the solar angle with the ice surface (Hughes, 1975) and variable katabatic winds that cause variable ablation rates.

Variations of φ in Fig. 10 suggest two locations for the grounding line of floating ice in Byrd Glacier fjord, one about 90 km from the start of the profiles where ice is 1100 m thick and the φ plots cross at $x \approx 80$ km for $A = 23\,\mathrm{bar\,a}^{1/3}$, and another at $x \approx 50$ km from the start where ice is 750 m thick and the φ plots cross for $A = 8\,\mathrm{bar\,a}^{1/3}$. Both locations satisfy the buoyancy requirement for floating ice. Tripling A makes ice too stiff, but apparently stiffer ice would also be produced by strong buttressing from the Ross Ice Shelf, which is the case since $\dot{\varepsilon}_{xx} \approx 0$ over the 40 km between these two possible grounding lines.

The threefold increase in A causes a very sharp reduction of $\dot{\varepsilon}_{xx}$ in Eq. (30). Indeed, Brecher (1982) found that $\dot{\varepsilon}_{xx} \approx 0$ at $x \approx 80$ km, which is close to the grounding line for floating ice in both Eqs. (34) and (38) with and without side shear, respectively. This is possible if extending stress σ_T for unbuttressed ice is 5.5 bars for ice 1100 m thick and 3.8 bars for ice 750 m thick in Eq. (48), so keeping $\dot{\varepsilon}_{xx} \approx 0$ in this region requires that σ_T is nearly balanced by buttressing back-stress σ_B in Eq. (49), giving $\sigma_\mathrm{T} \approx 0$ in Eq. (30).

CC BY

Then A can remain at 8 bar a$^{1/3}$ if some grounding between 1100 m at $x = 90$ km and 750 m at $x = 50$ km keeps φ around 0.8 instead of 1.0 or if buttressing by the Ross Ice Shelf is nearly total.

Thomas and MacAyeal (1982) calculated buttressing back-forces on the Ross Ice Shelf using data from the Ross Ice Shelf Geophysical and Glaciological Survey (RIGGS). Although their data did not include the floating part of Byrd Glacier, R. H. Thomas (personal communication, 16 March 2013) calculated that $\sigma_B \approx 4.7$ bars if $h_0 = 1100$ m at the grounding line and $\sigma_B \approx 3.0$ bars if $h_0 = 750$ m at the grounding line. His results are close enough to ours for us to conclude Byrd Glacier is almost fully buttressed by the Ross Ice Shelf. Equation (56) then gives $\varphi_O = 0$ with σ_U given by Eq. (48) for h_0 either 1100 m or 750 m at the ice-shelf grounding line where $\varphi_B = \varphi\varphi_O = 0$ in Eq. (58). This requires that $\psi = 0$ for no basal drag and $L_F \overline{h}_F \ll (L_G \overline{h}_G + C_R \overline{h}_R)$ in Eq. (57). These conditions on the Ross Ice Shelf are largely satisfied, since no ice rumples exist and the grounded length of all the many inlets along the Transantarctic Mountains, plus the grounded length of the Shirase, Siple, and Gould Coasts of West Antarctica, plus the circumference of ice rises, greatly exceed floating length L_F of the calving front.

Drainage of the two subglacial lakes reported by Stearns et al. (2008) was accompanied by a ten percent increase in the discharge velocity of ice across the ungrounding line of Byrd Glacier. For mass-balance continuity, this would require a ten percent reduction in ice thickness over time and a corresponding retreat of the ice-shelf grounding line up Barne Inlet. Initially, the grounding line should advance because ice having the present thickness would be moving ten percent faster. No data were obtained to measure ice-thickness changes. If eventual ice thinning increases linearly along Byrd Glacier to ten percent at the ungrounding line, the variation of φ along x is doubled or tripled, as shown in Fig. 11, using Eq. (20), which includes side shear against the fjord walls, and Eq. (36) for the centerline with side shear incorporated into basal shear, leading to Eqs. (34) and (38), respectively, with C_2 given by Eq. (62) for full ice-shelf buttressing. This did not happen, of course, because the discharged subglacial water

TCD
8, 2043–2118, 2014

crossed the ungrounding line before the ice surface could lower to accommodate the temporary reduction in ice-bed coupling.

6 Ice-shelf unbuttressing for Jakobshavn Isbrae

Jakobshavn Isbrae drains 5 to 7 % of the Greenland Ice Sheet (Bindschadler, 1984; Pelto et al., 1989) and ended in Jakobshavn Isfjord as a floating ice shelf about 10 km long and 6 km wide until the ice shelf disintegrated suddenly in 2002 (Joughin et al., 2008). Summer velocities are still increasing (Joughin et al., 2014). Jakobshavn Isbrae had retreated 27 km since 1850, the end of the Little Ice Age in Greenland, and its calving front had been relatively stable since 1964 (Weidick and Bennike, 2007). Since velocity measurements began in 1964, it has been the fastest-known ice stream on Earth (Carbonnell and Bauer, 1968). Surface elevations and velocities were mapped by aerial photogrammetry over a 100 km by 100 km area of ice converging on Jakobsavn Isfjord and on the ice shelf in 1985 and 1986 (Fastook and others, 1995; Prescott et al., 2003). The surface morphology and mass balance were studied extensively by Echelmeyer and others (1991, 1992) from 1985 to 1988. Temperatures were measured through Jakobshavn Isbrae by hot-water drilling in 1988 and 1989 (Iken et al., 1993; Funk et al., 1994). CReSIS mapped surface and bed topography by radar for Jakobshavn Isbrae and its ice catchment/drainage basin from 2004 to 2008. Jakobshavn Isbrae occupies a subglacial trench we informally call "Gogineni Gorge" that is fairly straight, 100 km long, 4 km wide, and up to 1500 m deep.

Figure 12 is a satellite image of Jakobshavn Isbrae showing the centerline along which floating fraction φ is calculated. Figure 13 is the CReSIS map of bed topography where ice converges on Jakobshavn Isfjord. "Gogineni Gorge" is clearly seen. Ice thickness approximately doubles in the gorge. The flowline shown in Fig. 13 follows the centerline of the gorge. Figure 13 shows profiles of the ice surface, base, and thickness along the centerline, and locates the (un)grounding line. Two surface and thickness profiles are shown, one in 1985 before the buttressing ice shelf in Jakobshavn Isfjord disintegrated in 2002 and one in 2012 after the ice shelf disintegrated. Other profiles in 1993, 2003, and 2006 lie between these profiles and reflect transient events preceding and following disintegration (Hofstede and Hughes, 2013).

Ice rumples behind the ice-shelf calving front and side shear against the fjord walls allowed the ice shelf to buttress Jakobshavn Isbrae. Buttressing was nearly total, because longitudinal strain rate $\dot{\varepsilon}$ was nearly zero from the grounding line to the calving front (Prescott et al., 2003). The velocity increase and surface lowering that accompanied disintegration of the buttressing ice shelf in 2002 can be linked to a reduction in ice-shelf buttressing using $\dot{\varepsilon}$ in Eq. (30) to get $(\Delta h/\Delta x)_F$ in Eq. (29), with $h_O = 1000\,\mathrm{m}$ and $u_O = 7.0\,\mathrm{km\,a^{-1}}$ at $x = 0$ before disintegration (Prescott et al., 2003) and $h_O = 850\,\mathrm{m}$ and $u_O = 12.6\,\mathrm{km\,a^{-1}}$ at $x = 0$ after disintegration (Joughin et al., 2008). Fastook et al. (1995) measured velocities u before disintegration, for comparison with u obtained from Eq. (23) with h_I obtained from Fig. 14 for Gogineni Gorge, and used $A = 1.4 \times 10^5\,\mathrm{kPa\,s^{1/3}} = 4.43\,\mathrm{bar\,a^{1/3}}$, corresponding to an ice temperature averaging $-15\,^{\circ}\mathrm{C}$, which lies within measured temperatures ranging from -2 to $-22\,^{\circ}\mathrm{C}$ (Iken et al., 1993; Luthi et al., 2002). R. Thomas (personal communication, 22 April 2013) recommends $A = 2.5\,\mathrm{bar\,a^{1/3}}$ as a better fit with measured temperatures, so we prefer his value. For $(a - r)$, we set $a = 0.59\,\mathrm{m\,a^{-1}}$, following Bindschadler (1984), Pelto et al. (1989), and Echelmeyer et al. (1992), with r to be calculated from ice-surface lowering rates during and following disintegration of the buttressing ice shelf. For $(\Delta h/\Delta x)_G$ in Eq. (26), we took $B = 1.123 \times 10^4\,\mathrm{kPa\,s^{1/2}\,m^{-1/2}} = 0.02\,\mathrm{bar\,a^{1/2}\,m^{-1/2}}$ (Hofstede and Hughes, 2013), $L = 500\,\mathrm{km}$, and used h_I in Fig. 13 with $m = 2$ because ice thickness is measured directly. Then φ variations along x can be calculated from measured values of $C_1 = \Delta h/\Delta x$ and calculated values of $C_2 = (\Delta h/\Delta x)_F$ and $C_3 = (\Delta h/\Delta x)_G$ in Eqs. (34) and (38), respectively, with side shear in Gogineni Gorge and with side shear absorbed into basal shear along the ice-stream centerline.

Measured surface slopes $(\Delta h/\Delta x)$ in Eq. (32) can now be used to calculate variations of φ along x from Eqs. (34) and (38). These results are shown in Fig. 15, which

TCD
8, 2043–2118, 2014

also shows φ variations calculated from Eq. (21) using only the force balance. Reasonable limits to ice hardness parameter A have little effect on φ variations. Values of C_2 used to calculate φ obtained from Eqs. (34) and (38) are obtained from Eq. (61), with $f_B = 1$ for full buttressing giving Eq. (62) before ice-shelf disintegration, and $f_B = 0$ for no buttressing giving Eq. (63) after disintegration. Full buttressing is assumed, given the observation in 1985 that longitudinal strain rate $\dot{\varepsilon}_{xx} \approx 0$ from the grounding line to the calving front of the ice shelf (Prescott et al., 2003).

In 1985, variations of φ along x from Eqs. (34) and (38) are low after falling sharply from $\varphi = 1$ at the ungrounding line over the 5 km where Jakobshavn Isbrae has a concave surface profile, remaining in the range $0.1 < \varphi < 0.2$ with Eq. (34) for side shear giving the lower values as expected, but both rising to $\varphi = 0.8$ above the high bedrock hill at $14\,\text{km} < x < 22\,\text{km}$. The low φ values identify regions where stream flow is dominated by basal sliding of mostly grounded ice. Jakobshavn Isbrae is narrow, so side shear is also important (see Dupont and Alley, 2005a, b).

In 2012, variations of φ along x from Eqs. (34) and (38) are much higher all along x, mostly in the range $0.4 < \varphi < 0.8$ after falling from $\varphi = 1$ at the ungrounding line. Equation (34) for side shear again gives the expected lower φ values, but this time gives a high value of $\varphi = 0.7$ for $24\,\text{km} < x < 30\,\text{km}$ just before ice encounters the high bedrock hill. Eq. (38) without side shear gives $\varphi = 1$ over the range $14\,\text{km} < x < 30\,\text{km}$, which includes the high bedrock hill. Disintegration of the buttressing ice shelf in 2002 has enhanced linear shelf flow to equal or exceed basal sliding of grounded stream flow.

Equation (21) from the force balance alone has $\varphi = 1$ at the ungrounding line, then decreasing rapidly to $\varphi = 0.6$ in both 1985 and 2012, before rising to $\varphi = 0.9$ above the high bedrock hill before falling to between 0.4 and 0.5, with the lower values in 1012. This is because $h_O = 1000\,\text{m}$ in 1985 became $h_O = 850\,\text{m}$ in 2012 at $x = 0$. This ungrounding-line surface lowering exceeds lowering at locations $x > 0$. Disintegration of the buttressing ice shelf in 2002 has enhanced stream flow. Variations of φ along x in Fig. 15 obtained from Eqs. (34) and (38) using both the force balance and the mass balance show a sharp drop from $\varphi = 1$ to $0.1 < \varphi < 0.2$ over distance $x \approx 5$ km behind the ungrounding line in 1985, but falling to only $\varphi \approx 0.6$ in 2012, with large fluctuations, the same drop produced by Eq. (21) obtained from the force balance alone. This increase in φ has been accompanied by a fourfold summer velocity increase since 2009 and retreat of the grounding line into a subglacial depression, see Figs. 14 and 15 (Joughin et al., 2014).

7 Discussion of results

We examined the Jakobshavn Effect, observed on Jakobshavn Isbrae in Greenland, as possibly contributing to collapsing marine parts of ice sheets during terminations of Quaternary glaciation cycles (Hughes, 1986). Collapse was linked to reduced ice-bed coupling under ice sheets over time during transitions from slow sheet flow to fast stream flow to buttressing shelf flow. Our approach was based on the first-order dependence of ice-sheet thickness on the strength of ice-bed coupling, such that ice 3000 m high and 4000 m thick at an interior ice divide can lower to 100 m high and 1000 m thick when ice margins become afloat, and lower further to 30 m high and 300 m thick at the front of calving ice shelves, a 99 % reduction of ice elevations, all due to reduced ice-bed coupling. We began by characterizing ice-bed uncoupling as an increase in thawed fraction f of the bed for sheet flow, of floating fraction φ of ice for stream flow, and of unbuttressed fraction φ_O of ice for shelf flow.

Results for sheet flow have been presented in broad regions of the Antarctic Ice Sheet where accurate data are available (Hughes, 1998, Chapter 3; Wilch and Hughes, 2000; Hughes, 2012, Chapter 24). It is encouraging that subglacial lakes are concentrated in regions where the bed was determined to be wholly thawed using this approach (Siegert, 2001; Smith et al., 2009). We now know that sheet flow consists of tributaries converging on ice streams, as shown in Fig. 1 for the Antarctic Ice sheet. In this study, we limit thawed beds ($f = 1$) to ice-stream tributaries, with frozen beds ($f = 0$) between tributaries, and we present new yield criteria that link ice elevations

cc BY

to ice-flow under both conditions. When ice is frozen to the bed, we invoked a yield criterion with yielding occurring at a critical strain rate in ice. When the bed thawed, we invoked a yield criterion with a lower yield stress linked to basal sliding over wet deforming till. Using Eq. (5) and Fig. 2, decreases in ice hardness represented by A due to increasing temperature and development of an easy-glide ice fabric near the bed are transferred to increasing exponent n if A is kept constant. As n increases, downslope ice velocities become increasingly constant through the ice thickness, with velocity increases confined to ice sliding over wet deforming till at the bed. These conditions we assign to ice tributaries where the bed is thawed, keeping lower values of n confined between tributaries where the bed is frozen. Ice-bed coupling is reduced when a frozen bed thaws, allowing tributaries to develop. Our approach can be rigorously tested using more robust ice-sheet models that link ice elevations to basal thermal and hydrological conditions that control ice-bed coupling over time for sheet flow in the map plane.

Results for stream flow were more problematic. A longitudinal geometrical force balance and a simplified mass balance were used to calculate floating fraction φ for stream flow. This approach departs from the usual practice of integrating the Navier–Stokes equilibrium equations for the force balance, using comprehensive ice accumulation and ablation equations for the mass balance, and solving equations for the energy balance to obtain internal ice temperatures and basal thermal conditions that control subglacial hydrology, all in three dimensions over time. In sharp contrast, we use a first-order approach that depends on ice elevations above the bed being determined primarily by the strength of ice-bed coupling along ice flowlines at present (Hughes, 2012).

Results for shelf flow are closely linked to results for stream flow, as required for the Jakobshavn Effect. Since ice shelves that buttress ice streams typically exist in confining embayments and are locally grounded on the bed at ice rises and ice rumples, our analysis is conducted in the map plane, unlike our essentially linear analysis for stream flow. We applied the two yield criteria we developed for internal shear and basal sliding in sheet flow to buttressing shelf flow, with ice shearing along the sides of embayments

cc BY

and around ice rises and ice sliding beneath ice rumples. This allowed us to link ice-shelf buttressing to the grounded and floating geometry of ice shelves, and eliminate stresses in determining the unbuttressed fraction φ_O of an ice shelf.

We had to make several assumptions to obtain solutions for sheet, stream, and shelf flow. Two are particularly important. For sheet and stream flow, we approximated the bed by an up-down staircase, with changes in bed topography put between steps, so normal stresses in the direction of ice flow pushed against "up" steps and pulled away from "down" steps. Bed slopes have to be less than 30°, so these normal stresses can be ignored compared to the gravitational driving stress (Hughes, 2012, Appendix E). Other stresses resisting gravitational forcing are all dependent on floating fraction φ of ice in an ice stream and its longitudinal gradient $\partial\varphi/\partial x$. We put gradients $\partial\varphi/\partial x$ between steps of constant length Δx, as with elevation changes Δh_B in bed topography. Then φ must vary slowly along x. However, surface slopes are rugged for Byrd Glacier and Jakobshavn Isbrae, and this produces rapid changes in φ along x that can overwhelm changes due to variations in ice-bed coupling, see Eqs. (32) and (36). Therefore we had to artificially smooth the ice surface using a running mean surface slope. This introduced uncertainty in our results. For stream flow, Eq. (34) for flowbands and Eq. (38) for flowlines gave multiple solutions for φ. We accepted solutions only for $0 \leq \varphi \leq 1$. If gradients of φ had been included, other φ variations are likely, even with a smoothed ice surface.

Our geometrical force balance is linked to a simple first-order mass balance given by Eq. (22) for linear ice flow, as illustrated in Fig. 7. Ice converges strongly on both Byrd Glacier and Jakobshavn Isbrae, but converging flow is not included in Eq. (22). However, our yield stress using separate yield criteria for sliding under tributaries and creep between tributaries in converging sheet flow has a weak dependence on surface accumulation rate a and thinning rate r, so our simplified mass balance is acceptable (Hughes, 2012, Appendix O). For Byrd Glacier, flow is largely linear except in the uppermost region where stream flow begins. Input ice flux at the beginning of stream flow is $h_S u_S$ in Fig. 7, so the mass-balance equation can be written $h_I u = h_S u_S - (a-r)(S-x)$

where u and u_S are negative with x positive upstream. Then $h_S u_S$ can be equated with $(a-r)$ averaged over the entire accumulation catchment area drained by Byrd Glacier.

The situation is more complex for Jakobshavn Isbrae. Ice flow within "Gogineni Gorge" is largely parallel because the gorge width is relatively constant. However ice flow above the gorge is strongly convergent. What is to be done? We used the average ice accumulation rate over the accumulation catchment area of Jakobshavn Isbrae to obtain an effective ice flux converging above the gorge, but confined to the width of the gorge, and add that flux to the relatively parallel ice flux inside the gorge itself. If ice in the upper part moves much faster than ice in the lower part, it should "pull" the lower ice. The result may be a temperate ice layer just above the bed that allows ice flow in the gorge to move faster, a possibility favored by Iken et al. (1993) from their temperature profiles. Converging sheet flow dominated by basal sliding may have prevailed in 1985 when $\varphi \approx 0.15 \pm 0.05$ before the buttressing ice shelf disintegrated in 2002, as seen in Fig. 14. After disintegration, stream flow in the gorge accelerated and may now "carry" the overlying converging sheet flow, since $\varphi \approx 0.5 \pm 0.1$ in 2012 a decade after the ice shelf disintegrated. High φ values as ice approaches and then passes over the high bedrock riegel suggests extrusion flow in the gorge, as Hooke et al. (1987) found on Storglaciaren in Sweden, despite objections by Nye (1952b). Greater ice-bed uncoupling may be caused by high pressure-melting rates in basal ice pushing against the riegel, especially when ice accelerates after the ice shelf disintegrates and buttressing vanishes.

We obtained surface and bed topography, and ice thickness, directly from radar echograms. Morlighem et al. (2013) compare methods for getting these data, and favor the mass conservation method. This method is unreliable for Byrd Glacier and Jakobshavn Isbrae because of difficulties noted above. CReSIS glaciologists (2014) will defend the method we used.

The nearly doubling of Jakobshavn velocity in the 27 years from 1985 to 2012 is accompanied by 150 m of surface lowering at the ungrounding line, giving an ice thinning rate of $r = 0.18\,\mathrm{m\,a^{-1}}$ compared with our ice accumulation rate of $a = 0.59\,\mathrm{m\,a^{-1}}$. How-

CC BY

ever, there was significant measured variability in r along x both positive (thinning) and negative (thickening) during these 27 years. We attribute this variability to unsettled ice dynamics in the years just before and just after the ice shelf disintegrated in 2002. We chose the years 1985 and 2012 to avoid these transient events and thereby capture longer-term trends.

A concern exists on how to treat floating fraction φ along ice streams and buttressing factor φ_O for a confined and pinned ice shelf supplied by the ice stream. Equations (34) and (38) are used to calculate φ, with term C_2 obtained from Eqs. (29) and (30), yet σ_T in Eq. (30) does not contain φ^2, unlike σ_T in Eq. (12) for ice streams. The reason for omitting φ^2 in Eq. (30) is it applies only to the floating fraction of ice in an ice stream, for which $\varphi = 1$. However, if φ^2 is included, then C_2 includes φ raised to the $2n+2$ power, giving φ^8 for $n = 3$. Then φ has eight solutions, among which only those with $0 \leq \varphi \leq 1$ can be used. This alternative was employed by Hofstede and Hughes (2013) for Jakobshavn Isbrae. It led to φ values that decrease irregularly from $\varphi = 1$ at the ungrounding line, $x = 0$, to $\varphi \approx 0.5 \pm 0.1$ at $x = 70$ km upstream. Their values generally exceed our φ values obtained from the φ^2 term in C_2 for 1985, but compare with our φ values for 2012. The big difference is φ values over the high bedrock riegel, a feature absent from bed topography used by Hofstede and Hughes (2013).

If the φ^2 dependence of $(\Delta h/\Delta x)_F = C_2$ is retained, as in Eq. (32), the opportunity is opened for converting φ in Eq. (12) into φ_O for ice-shelf buttressing. This leads to Eq. (61), with $f_B = 1$ for full ice-shelf buttressing and $f_B = 0$ for no ice-shelf buttressing, the two conditions we have for Jakobshavn Isbrae before and after the ice shelf disintegrated in 2002. Is this justified? We cannot be sure. However, if a confined and pinned ice shelf is not so different from an ice stream, as Thomas (2004) maintains, then the φ^2 term in Eq. (12) can be related to some form of ice-shelf buttressing that can be expressed by buttressing fraction f_B. This may account for values of $0.8 < \varphi < 0.9$ as Byrd Glacier becomes afloat when $A = 8\,\mathrm{bar\,a}^{1/3}$ is the ice hardness parameter. Making $\varphi = 1$ at the ungrounding line requires tripling A. The seemingly stiffer ice is equivalent to some partial grounding of floating ice over the 40 km where $\dot{\varepsilon}_{xx} \approx 0$ between possible

CC BY

ungrounding lines at $x = 50$ km where $h_O = 750$ m and at $x = 90$ km where $h_O = 1100$ m or, more likely, by nearly full buttressing from the Ross Ice Shelf.

We postulate that an ice shelf differs from an ice stream mainly in that water flows freely beneath an ice shelf, even when the ice shelf is confined in an embayment and has basal pinning points that produce ice rises and ice rumples on the ice surface, whereas water flowing under an ice stream encounters resistance from grounded regions beneath ice streams, as seen in Fig. 5. This resistance reduces a buttressing effective longitudinal "water" stress σ_W in an ice stream that is maximized for fully floating ice and vanishes for fully grounded ice. Partial grounding on the bed increases the thickness of an ice stream, and provides the resistance to free flow of basal water from sources to sinks, the main sink being under an ice shelf toward which basal water flows. This "water" stress σ_W is not readily recovered from solving the standard Navier–Stokes equilibrium equations. For this reason, its existence is questioned by many conventional ice-sheet modelers. Evidence supporting the existence of σ_W is the observation by Kamb (2001) that basal water under West Antarctic ice streams rises in boreholes to heights far above sea level, but attaining a height at the drilling sites that would "float" ice that is about 90 % of the observed ice height above the bed.

Another difference between stream flow and shelf flow is flow in ice shelves is generally two-dimensional, diverging and converging in the map plane, whereas flow in ice streams is primarily one-dimensional along nearly parallel flowlines. We treated this distinction by developing a force balance for ice shelves in the map plane in which resistance is determined by the fraction of the ice-shelf area that is grounded to produce ice rises and ice rumples, and the length of the ice-shelf perimeter that is grounded in an embayment compared to the freely-floating length along a calving front. In this force balance, resistance to shelf flow is provided by side shear stresses around ice rises and along sides of the embayment, and basal shear over the area of ice rumples. Side shear was equated with $\tau_S = 0.667\sigma_O$ and basal shear was equated with $\tau_O = 0.386\sigma_O$ in Fig. 2, where $\sigma_O = 100$ kPa = 1 bar is the plastic yield stress for ice. This allows resisting stresses to be eliminated from the solution and leads to Eqs. (53) and (56) for

TCD
8, 2043–2118, 2014

ice-shelf buttressing factor φ_O. Equation (53) allows φ_O to be estimated merely from ice-shelf geometry: its shape, the location, size, and shape of its ice rises and ice rumples, and the grounded and floating lengths of its perimeter (Hughes, 2012, Chapter 13).

Equation (4) plotted in Fig. 2 has two applications. First, it is used to illustrate two viscoplastic yielding criteria for slow sheet flow, one for creep in ice with a higher viscoplastic yield stress linked to a single strain rate measured in glacier ice and ice-cemented till for creep over frozen parts of the bed, and one with a lower viscoplastic yield stress and strain rate when melting allows basal ice to slide and mobilizes till over thawed parts of the bed. Second, the higher viscoplastic yield stress is applied to creep in cold ice shearing around basal pinning points that produce ice rises on an ice shelf, and the lower viscoplastic yield stress is applied to sliding of temperate ice over basal pinning points that produce ice rumples on the ice shelf. These ad hoc applications are used until the physics for these processes is adequately quantified.

If solutions of Eqs. (32) and (36) are real numbers between zero and one, we calculated them using Eqs. (34) and (38). If the solutions are complex numbers, or real numbers not in the zero-to-one range, we find approximate solutions of Eqs. (32) and (36) using a variation of a dissection method. The method consists of dividing the segment 0,1 into 1000 points and calculating absolute values of the quadratic functions, Eqs. (32) and (36), at each of these points. The point on the segment 0,1 which generates the smallest value of the corresponding function is accepted as the solution of this function. The method always generates an answer between zero and one, but does not satisfy the equation exactly. An example of this approach is seen in Fig. 14 for the 2012 values $\varphi = 1$ in Eq. (38) for the high bedrock riegel in "Gogineni Gorge".

For Byrd Glacier with $A = 8\,\mathrm{bar\,a}^{1/3}$, we found that floating fraction φ of ice fell from $\varphi \approx 0.8$ with side shear, Eq. (34), and $\varphi \approx 0.9$ without side shear, Eq. (38), for an ungrounding line at $x \approx 50\,\mathrm{km}$ where $h_O = 750\,\mathrm{m}$, to $\varphi \approx 0.1$ about 40 km upstream from this ungrounding line, and then φ increased slowly in an irregular manner to the head of the ice stream. An unreasonably high $A = 23\,\mathrm{bar\,a}^{1/3}$ enforces $\varphi = 1$ at

CC BY

the ungrounding line, which moves to $x \approx 90$ km where $h_O = 1100$ m. The upstream behavior is the same, but the rapid drop in φ is displaced 30 km upstream before φ stabilizes irregularly at around $\varphi \approx 0.1$, with φ then climbing to 0.4 at the head of Byrd Glacier when side shear is included. In both cases, basal sliding dominates stream flow along most of Byrd Glacier. We attribute the great thickness of Byrd Glacier to basal sliding and to nearly complete buttressing by the Ross Ice Shelf. Strong ice-shelf buttressing would have the same effect on reducing $\dot{\varepsilon}_{xx}$ to nearly zero in this region as obtained by increasing A to stiffen ice. Values of φ double or triple all along Byrd Glacier for only a ten percent increase in ice discharge velocity across the ungrounding line if ice thickness is allowed to decrease linearly by ten percent from zero at the head of Byrd Glacier. This would require a continuous supply of basal water comparable to that supplied by the two subglacial lakes for a short time. Eq. (21) from the force balance alone gives consistently higher φ values all along Byrd Glacier after decreasing from $\varphi = 1$ at the ungrounding line.

For Jakobshavn Isbrae with $A = 2.5\,\mathrm{bar\,a}^{1/3}$ in Eqs. (34) and (38), we found that stream flow dominated by basal sliding prevailed in 1985 before the buttressing ice shelf disintegrated in 2002, but linear shelf flow had become equally important by 2012. Stream flow with higher φ values was more important in both years without side shear, as expected, because side shear requires side grounding of ice. Ice elevations are progressively lower closer to the ungrouding line in 2012 compared to 1985, due to doubling the ice discharge velocity, but ice elevations are slightly higher farther upstream. We attribute this to thick upstream ice being advected downstream by the faster ice velocity after ice-shelf disintegration eliminated ice-shelf buttressing. With only the force balance, Eq. (21) gives considerably higher values of φ in 1985 than do Eqs. (34) and (38) that also include the mass balance, but by 2012 the φ values are comparable. However, φ from Eq. (21) is somewhat lower in 2012 compared to 1985. This is because $h_O = 1000$ m in 1985 and $h_O = 850$ m in 2012, due to greater lowering at $x = 0$ that began at $x > 0$. Our results follow from the assumption made in deriving Eq. (21) that applies primarily to stream flow for which $h_O < h_I$. The reduction of h_O

occurs because buttressing back-stress σ_B vanishes when the ice shelf disintegrates, see Eq. (50).

Our results for both Byrd Glacier and Jakobshavn Isbrae are compatible with basal buoyancy factor $\varphi_B = \varphi\varphi_O$ in Table 1 used to quantify the Jakobshavn Effect by making it the product of fraction φ linked to ice-bed uncoupling and fraction φ_O linked to ice-shelf unbuttressing. Uncoupling occurs when surface meltwater floods the bed. Unbuttressing occurs when a confining ice shelf disintegrates. We postulate that these two effects acting in tandem are sufficient to collapse marine portions of an ice sheet, and to that extent contribute to termination of glaciation cycles during the Quaternary Ice Age in which we now live. We found that neither of these two effects is active over the long term for Byrd Glacier in Antarctica, but both may have a long-term impact on Jakobshavn Isbrae in Greenland. The analysis by Schoof (2010) points to a temporary acceleration and thinning of Jakobshavn Isbrae now underway that could continue for a century (Joughin et al., 2014), much longer than the temporary acceleration of Byrd Glacier when the subglacial lakes drained (Stearns et al., 2008).

The positive feedbacks in the Jakobshavn Effect we quantified here depend on two processes. One process is surface meltwater reaching the bed and increasing ice velocity by reducing ice-bed coupling, a process reported by Zwally et al. (2002) near Jakobshavn Isbrae, and now called the Zwally Effect. It had been more rigorously demonstrated by others, notably by Iken (1981) theoretically and by Iken and Bindschadler (1986) on Findelengletscher in the Swiss Alps. The other process, analyzed by Thomas (2004), is accelerated discharge by Jakobshavn Isbrae after its buttressing ice shelf disintegrated catastrophically in 2002. Therefore, we have called this the Thomas Effect, although Weertman (1957a, 1974) laid the foundation. Surface meltwater reaching the bed reduces ice-bed coupling in the Jakobshavn Effect. This does not happen for Byrd Glacier, so as a proxy we used rapid discharge from two upstream subglacial lakes to reduce ice-bed coupling (Stearns et al., 2008).

The Jakobshavn Effect, bracketed by the Zwally Effect and the Thomas Effect, is shown in Table 1. Here φ quantifies ice-bed uncoupling under an ice stream and φ_O

quantifies ice-shelf unbuttressing beyond the ice stream. Both increase from zero to unity as uncoupling and unbuttessing increase from minimum to maximum. The positive feedback mechanisms in the Jakobshavn Effect all cause changes in φ and φ_O through time. Table 1 suggests the possibility the Jakobshavn Effect may characterize terminations of glaciation cycles during the Quaternary Ice Age. Various paths can be taken by φ and φ_O in going from zero to one, including reversals. This allows stadial-interstadial transitions as well as terminations of Quaternary glaciation cycles. We propose that Table 1 be used as a guide when studying ice streams in Greenland and Antarctica to determine where they may be placed in the "life cycle" of ice streams proposed by Hughes (2011) and applied to major Antarctic ice streams today. Life cycles, including reversals, have been documented in detail for Kamb Ice Stream by Engelhardt and Kamb (2013).

The gravitational driving stresses in Eq. (1) for linear sheet flow and in Eq. (48) for linear shelf flow were first derived analytically, see Nye (1952a) and Weertman (1957a), respectively, but they are also derived geometrically (Hughes, 2011). Derivations of gravitational driving stresses and resisting stresses for linear stream flow can also be done analytically/numerically (e.g., Pattyn, 2003; Sargent, 2009; Blatter et al., 2011) and geometrically (Hughes, 2012). There is no inherent contradiction between the analytical/numerical and geometrical approaches.

The modeling approach presented here, using geometry instead of partial differential equations, will not displace the standard approach using continuum mechanics. It is essentially one-dimensional along ice flowlines. Making it two-dimensional in the map plane would require giving the two-dimensional triangles and rectangle in Fig. 5 three dimensions by including variable widths to capture diverging and converging flow. This becomes too cumbersome and obscures the visual simplicity of using common geometrical shapes to illustrate gravitational and resisting forces in the force balance. Although a simple mass balance is included, our work is basically a force balance which is unsuited to studying changing ice dynamics through time. It captures "snapshots" of ice-bed coupling in time that determine ice elevations to an acceptable first-order

cc BY

accuracy. As such, it provides a useful way to visualize the force balance for those unfamiliar with manipulating partial differential equations, and provides an additional insight for those who have this expertise. Our approach provides a “teaching model” that can be used to introduce the more rigorous approach using continuum mechanics, and then perhaps also to provide physical insights not easily visualized by relying only on partial differential equations. The geometrical approach is suited to “bottom-up” modeling in which ice elevations are determined primarily by the strength of ice-bed coupling, deduced from glacial geology for former ice sheets. The analytical approach is suited to “top-down” modeling in which ice elevations are determined primarily by the surface mass balance, deduced from climate models for former ice sheets. Fastook and Hughes (2013) apply both approaches to Northern Hemisphere ice sheets during Quaternary glaciation cycles.

8 Conclusions

We examined the hypothesis that positive feedback mechanisms in marine ice streams, collectively called the Jakobshavn Effect, may characterize terminations of glaciation cycles during the Quaternary Ice Age (Hughes, 1986). Our applications to Byrd Glacier in Antarctica and to and Jakobshavn Isbrae in Greenland impose severe limitations on this possibility. To examine the possibility we separate these feedbacks into two broad categories, reductions in ice-bed coupling under ice streams due to surface meltwater reaching the bed, and reductions in ice-shelf buttressing beyond the ice stream due to enhanced melting and calving of ice. The product of these two effects, an increase in floating fraction φ of ice under ice streams and an increase in the unbuttressed fraction φ_O of ice beyond ice-shelf grounding lines, is a basal buoyancy factor $\varphi_B = \varphi\varphi_O$. Hughes (2011) attempted to quantify φ_B during proposed “life cycles” of Antarctic ice streams consisting of inception, growth, mature, declining, and terminal stages as shown in Table 1.

CC BY

Byrd Glacier, Antarctica's ice stream having the largest catchment area, has low values of φ and φ_O. Jakobshavn Isbrae, Greenland's fastest ice stream, has high values of φ and φ_O. These conditions bracket those existing for marine ice streams in general. For Byrd Glacier we used φ to quantify ice-bed uncoupling when two subglacial lakes at its head drained rapidly in 2007 (Stearns and others, 2008), since surface meltwater does not reach the bed. For Jakobshavn Isbrae, we used φ_O to quantify unbuttressing when its buttressing ice shelf disintegrated catastrophically in 2002 (Thomas, 2004). For both ice streams, we found no reason to believe the Jakobshavn Effect would go to completion by collapsing marine portions of their ice drainage basins, such that φ_B might approach unity for environmental conditions now or in the foreseeable future. Our conclusion need not apply to major marine ice streams of former ice sheets. Our results are consistent with Table 1, which shows many paths of φ and φ_O through time, including reversals, with few paths leading to terminations of Quaternary glaciation cycles.

Warming in high polar latitudes can, in principle, trigger the Jakobshavn Effect. For Greenland, it would move northward along the east and west coasts, affecting all calving ice streams. For Antarctica, it would affect the northernmost ice streams, which are primarily in East Antarctica, But Thwaites Glacier and Pine Island Glaciers entering the Pine Island Bay polynya in West Antarctica may also be affected, see Pingree et al. (2011). Hughes (2011) has tentatively assigned inception, growth, mature, declining, and terminal life-cycle stages in Table 1 to Antarctic ice streams at the present time, using Eq. (21).

Acknowledgements. Funding for this work was provided by the Center for Remote Sensing of Ice Sheets (CReSIS) at the University of Kansas, under contracts with the US National Science Foundation (NSF) and the US National Aeronautical and Space Administration (NASA). R. Thomas of NASA provided valuable input to our work. M. Truffer and J. Bassis provided superb reviews of all aspects of our work, and made numerous recommendations that we have incorporated. Our debt to them is enormous.

References

Anandakrishnan, A. and Alley, R. B.: Tidal forcing of basal seismicity of ice stream C, West Antarctica, observed far inland, J. Geophys. Res., 102, 15183–15196, 1997.

Bindschadler, R. A.: Jakobshavns Glacier drainage basin: a balance assessment, J. Geophys. Res., 89, 2066–2072, 1984.

Blatter, H.: Velocity and stress fields in grounded glaciers: a simple algorithm for including deviatoric stress gradients, J. Glaciol., 41, 333–344, 1995.

Blatter, H., Greve, R., and Abe-Ouchi, A.: Present State and Prospects of Ice Sheet and Glacier Modelling, Surv. Geophys., Springer, New York City, 2011.

Bougamont, M., Price, S., Christoffersen, P., and Payne, A. J.: Dynamic patterns of ice stream flow in a 3-D higher-order ice sheet model with plastic bed and simplified hydrology, J. Geophys. Res., 116, F04018, doi:10.1029/2011JF002025, 2011.

Brecher, H. H.: Photogrammetric determination of surface velocities and elevations on Byrd Glacier, Anarct. J. US., 17, 79–81, 1982.

Budd, W. F., Jensen, D., and Radok, U.: Derived Physical Characteristics of the Antarctic Ice Sheet, University of Melbourne, Meteorology Department Australian National Antarctic Research Expeditions (ANARE) Interim Reports, Series A (IV), Glaciology, 120, 1971.

Bueler, E. and Brown, J.: Shallow shelf approximation as a “sliding law” in a thermomechanically coupled ice sheet model, J. Geophys. Res., 114, F03008, doi:10.1029/2008JF001179, 2009.

Carbonnell, M. and Bauer, A.: Exploitation des couvertures photographiques aériennes répétées du front des glaciers vêlant dans Diske Bugt en Umanak Fjord, Juin–Juillet, 1964, Meddelelser om Groenland, 173, 1–78, 1968.

Carlson, A. E., Jenson, J. W., and Clark, P. U.: Modeling the subglacial hydrology of the James Lobe of the Laurentide Ice Sheet, Quaternary Sci. Rev., 26, 1384–1397, doi:10.1016/j.quascirev.2007.02.002, 2007.

Clark, P. U.: Surface form of the southern Laurentide Ice Sheet and its implications to ice-sheet dynamics, Geol. Soc. Am. Bull., 104, 595–605, 1992.

Denton, G. H. and Hughes, T. J. (Eds.): The Last Great Ice Sheets, Wiley-Interscience, New York, 1981.

Drewry, D. J.: Antarctica: Glaciological and Geophysical Folio, Scott Polar Research Institute, University of Cambridge, Cambridge, 1983.

Dupont, T. and Alley, R. B.: Assessment of the importance of ice-shelf buttressing to ice-sheet flow, Geophys. Res. Lett., 32, L04503, doi:10.1029/2004GL022024, 2005.
Dupont, T. and Alley, R. B.: The importance of small ice shelves in sea-level rise, Geophys. Res. Lett., 33, L09503, doi:10.1029/2005GL025665, 2006.
Echelmeyer, K., Clarke, T. S., and Harrison, W. D.: Surficial glaciology of Jakobshavns Isbræ, West Greenland: Part I. surface morphology, J. Glaciol., 37, 368–382, 1991.
Echelmeyer, K., Harrison, W. D., Clarke, T. S., and Benson, C.: Surficial glaciology of Jakobshavns Isbræ, West Greenland: Part II. ablation, accumulation and temperature, J. Glaciol., 38, 169–181, 1992.
Engelhardt, H. and Kamb, B.: Ice stream flow history and surge potential, Ann. Glaciol., 54, 287–298, 2013.
Fastook, J. L. and Hughes, T. J.: New perspectives on paleoglaciology, Quaternary Sci. Rev., 80, 169–194, 2013.
Fastook, J. L. and Prentice, M.: A finite-element model of Antarctica, sensitivity test for meteorological mass–balance relationship, J. Glaciol., 40, 167–175, 1994.
Fastook, J. L., Brecher, H. H., and Hughes, T. J.: Derived bedrock elevations, strain rates, and stresses from measured surface elevations and velocities: Jakobshavn Glacier, Greenland, J. Glaciol., 41, 161–173, 1995.
Funk, M., Echelmeyer, K., and Iken, A.: Mechanisms of fast flow in Jakobshavns Isbrae, West Greenland: Part II. modeling of englacial temperatures, J. Glaciol., 40, 569–585, 1994.
Gagliardini, O., Durand, G., Zwinger, T., Hindmarsh, R. C. A., and Le Meur, E.: Coupling of ice-sheet melting and buttressing is a key process in ice-sheet dynamics, Geophys. Res. Lett., 37, L14501, doi:10.1029/2010GL043334, 2010.
Glen, J. W.: The flow law of ice, International Association of Scientific Hydrology, 47, 171–183, 1858.
Gow, A. J., Meese, D. A., Alley, R. B., Fitzpatrick, J. J., Anandakrishnan, S., Woods, G. A., and Elder, B. C.: Physical and structural properties of the Greenland Ice Sheet Project 2 ice cores: a review, J. Geophys. Res., 102, 26559–26575, 1997.
Greve, R.: A continuum-mechanical formulation for shallow polythermal ice sheets, Philos. T. Roy. Soc. A, 355, 921–974, doi:10.1098/rsta.1997.0050, 1997.
Hofstede, C. and Hughes, T.: Can ice sheets self-destruct and cause rapid climate change?, A case study: Jakobshavn Isbrae, Greenland, in: Atmosphre and Climate: Physics, Compo-

sition/Dynamis and Health Impacts, edited by: Wright, A. and Johnnson, S., Nova Science Publishers Inc., Hauppauge, NY, 1–33, 2013.
Holland, D. R., Thomas, R., de Young, B., Ribergaard, M., and Lyberth, B.: Acceleration of Jakobshavn Isbrae triggered by warm subsurface ocean waters, Nat. Geosci., 1, 659–664, doi:10.1038/ngeo316, 2008.
Hughes, T.: Ice Streamline Cooperative Antarctic Project, ISCAP Bulletin No. 1: Scientific Justification, Institute of Polar Studies, The Ohio State University, 1972.
Hughes, T.: Is the West Antarctic Ice Sheet disintegrating?, J. Geophys. Res., 78, 7884–7910, 1973.
Hughes, T.: A differential ablation-longitudinal compression mechanism for generating wave trains on cold alpine glaciers, in: Snow and Ice Symposium – Neiges et Glaces (Proceedings of the Moscow Symposium, August 1971, Actes du Colloque de Moscou, aout 1971), IASH – AISH Publication Number 104, 1975.
Hughes, T.: The Jakobshavns Effect, Geophys. Res. Lett., 13, 46–48, 1986.
Hughes, T.: On the pulling power of ice streams, J. Glaciol., 38, 125–151, 1992.
Hughes, T.: Ice Sheets, Oxford University Press, New York, 1998.
Hughes, T. J.: The geometrical force balance in glaciology, J. Geophys. Res., 108, NO.B11,2526, doi:10.1029/2003JB002557, 2003.
Hughes, T.: Variations of ice-bed coupling, beneath and beyond ice streams, J. Geophys. Res., 114, BO1410, doi:10.1029/2008JB005714, 2009.
Hughes, T.: A simple holistic hypothesis for the self-destruction of ice sheets, Quaternary Sci. Rev., 30, 1829–1845, 2011.
Hughes, T.: Holistic Ice Sheet Modeling: A First-Order Approach, Nova Science Publishers Inc., Hauppauge, New York, 2012.
Hughes, T., Sargent, A., and Fastook, J.: Ice-bed coupling beneath and beyond ice streams: Byrd Glacier, Antarctica, J. Geophys. Res., 116, 1–17, 2011.
Iken, A.: The effect of subglacial water pressure on the sliding velocity of a glacier in an idealized numerical model, J. Glaciol., 27, 407–422, 1981.
Iken, A. and Bindschadler, R. A.: Combined measurements of subglacial water pressure and surface velocity of Findelengletscher, Switzerland: conclusions about drainage system and sliding mechanism, J. Glaciol., 32, 101–119, 1986.

CC BY

Iken, A., Echelmeyer, K., Harrison, W., and Funk, M.: Mechanics of fast flow in Jakobshavns Isbrae, West Greenland: Part I. measurements of temperature and water level in deep boreholes, J. Glaciol., 39, 15–25, 1993.
Jenson, J. W., Clark, P. U., MacAyeal, D. R., Ho, C. L., and Vela, J. C.: Numerical modeling of advective transport of saturated deforming sediment beneath the Lake Michigan Lobe, Laurentide Ice Sheet, Geomorphology, 14, 157–166, 1995.
Jenson, J. W., MacAyeal, D. R., Clark, P. U., Ho, C. L., and Vela, J. C.: Numerical modeling of subglacial sediment deformation: implications for the behavior of the Lake Michigan Lobe, Laurentide Ice Sheet, J. Geophys. Res., 101, 8717–8728, 1996.
Joughin, I. R., Howat, I. M., Fahnestock, M. A., Smith, B., Krabill, W. B., Alley, R. B., Stern, H., and Truffer, M.: Continued evolution of Jakobshavn Isbrae following its rapid speedup, J. Geophys. Res., 113, F04006, doi:10.1029/2008JF001023, 2008.
Joughin, I., Smith, B. E., Shean, D. E., and Floricioiu, D.: Brief Communication: Further summer speedup of Jakobshavn Isbræ, The Cryosphere, 8, 209–214, doi:10.5194/tc-8-209-2014, 2014.
Kamb, B.: Basal zone of the West Antarctic ice streams and its role in lubrication of their rapid motion, in: The West Antarctic Ice Sheet: Behavior and Environment, edited by: Alley, R. B. and Bindschadler, R. A., American Geophysical Union (Antarctic Research Series), Washington, DC, 157–200, 2001.
Larour, E., Setousi, H., Morlighem, M., and Rignot, E.: Continental scale, high order, high spatial resolution, ice sheet modeling using the Ice Sheet System Model (ISSM), J. Geophys. Res., 117, F01022, doi:10.s1029/2011JF002140, 2012.
Le Hooke, R., B., Holmlund, P., and Iverson, N. R.: Extrusion flow demonstrated by bore-hole deformation measurements over a riegel, Shorglaciaren, Sweden, J. Glaciol., 33, 72–78, 1987.
Lliboutry, L.: General theory of subglacial cavitation and sliding of temperate glaciers, J. Glaciol., 7, 21–58, 1968.
Lüthi, M., Funk, M., Iken, A., Gogineni, S. P., and Truffer, M.: Mechanism of fast flow in Jakobshavns Isbrae, West Greenland, Part III. Measurements of ice deformationm, temperpature and cross-borehole conductivity in boreholes to the bedrock, J. Glaciol., 48, 369–385, 2002.
MacAyeal, D. R.: Large-scale ice flow over a viscous basal sediment: theory and application to Ice Stream B, Antarctica, J. Geophys. Res., 94, 4071–4087, 1989.

TCD
8, 2043–2118, 2014
Quantifying the Jakobshavn Effect
T. Hughes et al.

Morlighem, M., Rignot, E., Mouginot, J., Wu, X., Larour, E., and Paden, J.: Bed topography of Russel Glacier, Greenland, inferred from mass conservation using Opeeration IceBridge data, J. Glaciol., 59, 1015–1023, 2013.
Nye, J. F.: The mechanics of glacier flow, J. Glaciol., 2, 82–93, 1952a.
Nye, J. F.: Reply to Mr. Joel E. Fischer's comments, J. Glaciol., 2, 52–53, 1952b.
Pattyn, F.: A new three-dimensional higher-order thermomechanical ice sheet model: basic sensitivity, ice stream development, and ice flow across subglacial lakes, J. Geophys. Res., 108, 2382, doi:10.1029/2002JB002329, 2003.
Pelto, M. S., Hughes, T. J., and Brecher, H. H.: Equilibrium state of Jakobshavns Isbrae, West Greenland, Ann. Glaciol., 12, 127–131, 1989.
Pfeffer, W. T. and Bretherton, C. S.: The effect of crevasses on the solar heating of a glacier surface, in: The Physical Basis of Ice Sheet Modeling (Proceeedings of the Vancouver Symposium, August 1987), IASH Publiction No. 170, 191–205, 1987.
Pingree, K., Lurie, M., and Hughes, T.: Is the East Antarctic Ice Sheet stable?, Quaternary Res., 75, 417–429, 2011.
Pollard, D. and DeConto, R. M.: Description of a hybrid ice sheet-shelf model, and application to Antarctica, Geosci. Model Dev., 5, 1273–1295, doi:10.5194/gmd-5-1273-2012, 2012.
Prescott, P. R., Kenneally, J. P., and Hughes, T. J.: Relating crevassing to nonlinear strain in the floating part of Jakobshavns Isbrae, West Greenland, Ann. Glaciol., 36, 149–156, 2003.
Pritchard, H. D., Arthern, D. G., Vaughan, D. G., and Edwards, L. A.: Extensie dynamic thinning on the margins of the Greenland and Antarctic ice sheets, Nature, 461, 803–806, doi:10.1038/Nature08471, 2009.
Rignot, E. and Kanagaratnam, P.: Changes in the velocity structure of the Greenland Ice sheet, Science, 311, 986–990, 2006.
Rignot, E., Casassa, G., Gogineni, P., Krabill, W., Rivera, A., and Thomas, R.: Accelerated ice discharge from the Antarctic Peninsula following the collapse of Larsen B ice shelf, Geophys. Res. Lett., 31, L18401, doi:10.1029/2004GL020697, 2004.
Rignot, E., Mouginet, J., and Scheichl, B.: NASA Research Yields Field Map of Antarctic Ice Flow, NASA News, available at: www.jpl.nasa.gov/news/news.cfmflrelease=2011-256&cid=release (last access: 19 September 2013), 2011a.
Rignot, E., Mouginot, J., and Scheuchl, B.: Ice flow of the Antarctic Ice Sheet, Science, 333, 1427–1430, 2011b.

CC BY

Rowden-Rich, R. J. M. and Wilson, C. J. L.: Models for strain localization in Law Dome, East Antarctica, Ann. Glaciol., 23, 396–401, 1996.
Saito, F. and Abe-Ouchi, A.: Sensitivity of Greenland ice sheet simulation to the numerical procedure employed for ice-sheet dynamics, Ann. Glaciol., 42, 331–336, doi:10.3189/172756405781813069, 2005.
Sargent, A.: Modeling Ice Streams, Ph.D. thesis, University of Maine, Orono, 106 pp., 2009.
Sargent, A. and Fastook, J. L.: Manufactured analytical solutions for isothermal full-Stokes ice sheet models, The Cryosphere, 4, 285–311, doi:10.5194/tc-4-285-2010, 2010.
Scambos, T. A., Bohlander, J. A., Shuman, A., and Skvarca. P.: Glacier acceleration and thinning after ice shelf collapse in the Larsen B embayment, Antarctica, Geophys. Res. Lett., 31, L18402l, doi:10.1029/2004GL020670, 2004.
Sanderson, T. J. O.: Equilibrium profile of ice shelves, J. Glaciol., 22, 435–460, 1979.
Schoof, C.: Marine ice-sheet dynamics, Part 1. The case of rapid sliding, J. Fluid Mech., 573, 27–55, 2007.
Schoof, C.: Ice-sheet acceleration driven by melt supply variability, Nature, 468, 803–806, 2010.
Seddik, H., Greve, R., Zwinger, T., Gillet-Chaulet, F., and Gagliardini, O.: Simulations of the Greenland ice sheet 100 years into the future with the full Stokes model Elmer/Ice, J. Glaciol., 58, 427–440, doi:10.3189/2012JoG11J177, 2012.
Siegert, M. J.: Comments on "Calculating basal thermal zones beneath the Antarctic ice sheet" by Wilch and Hughes, J. Glaciol., 46, 159–160, 2001.
Smith, B. E., Fricker, H. A., Joughin, I. R., and Tulaczyk, S.: An inventory of active subglacial lakes in Antarctica detected by ICESat (2003–2008), J. Glaciol., 55, 573–595, 2009.
Stearns, L. A., Smith, B. E., and Hamilton, G. S.: Increased flow speed on a large East Antarctic outlet glacier due to subglacial floods, Nat. Geosci., 1, 827–831, 2008.
Swithinbank, C. W.: Ice movement of valley glaciers flowing into the Ross Ice Shelf, Antarctica, Science, 141, 523–524, 1963.
Thomas, R. H.: The creep of ice shelves: theory, J. Glaciol., 12, 45–53, 1973a.
Thomas, R. H.: The creep of ice shelves: interpretation of observed behaviour, J. Glaciol., 12, 55–70, 1973b.
Thomas, R. H.: Force-perturbation analysis of recent thinning and acceleration of Jakobshavns Isbrae, Greenland, J. Glaciol., 50, 57–66, 2004.

Thomas, R. H. and MacAyeal, D. R.: Derived characteristics of the Ross Ice Shelf, J. Glaciol., 28, 397–412, 1982.
Thomas, R. H., Rignot, E. J., Kanagaratnam, P., Krabill, W. B., and Casassa, G.: Force-perturbation analysis of Pine Island Glacier, Antarctica, suggests cause for recent acceleration, Ann. Glaciol., 39, 133–138, 2004.
Van der Veen, C. J.: A Note on the Equilibrium Profile of a Free Floating Ice Shelf, Institut voor Meteorologie en Oceanografie, 15, Rijksuniversiteit, Utrecht, the Netherlands, 1983.
Weertman, J.: Deformation of floating ice shelves, J. Glaciol., 3, 38–42, 1957a.
Weertman, J.: On the sliding of glaciers, J. Glaciol., 3, 33–38, 1957b.
Weertman, J.: Stability of the junction of an ice sheet and an ice shelf, J. Glaciol., 13, 3–11, 1974.
Weideck, A. and Bennike, O.: Quaternary Glaciation History and Glaciology of Jakobshavn Isbrae and the Disko Bugt Region, West Greenland: a Review, Ministry of Climate and Energy, Copenhagen, 78 pp., 2007.
Whillans, I. M., Chen, Y. H., Van der Veen, C. J., and Hughes, T.: Force Budget III: application to three-dimensional flow of Byrd Glacier, Antarctica, J. Glaciol., 35, 68–80, 1989.
Wilch, E. and Hughes, T.: Mapping basal thermal zones beneath the Antarctic ice sheet, J. Glaciol., 46, 297–310, 2000.
Zwally, H. J., Abdalati, W., Herring, T., Larson, K., Savba, J., and Steffen, K.: Surface melt-induced acceleration of greenland ice-sheet flow, Science, 297, 218–222, 2002.

Table 1. Quantifying the Jakobshavn Effect in a Life-Cycle Classification for Ice Streams.

↓Increasing ice-bed coupling	*Stages in life cycle*				
	1A	1B	1C	1D	1E
	2A	2B	2C	2D	2E
	3A	3B	3C	3D	3E
	4A	4B	4C	4D	4E
	5A	5B	5C	5D	5E
	Increasing ice-shelf buttressing→				

ZWALLY EFFECT ↑	*Stage*	*ϕ_B during life cycle*				
	Inception	1	3/4	1/2	1/4	0
	Growth	3/4	9/16	3/8	3/16	0
	Mature	1/2	3/8	1/4	1/8	0
	Declining	1/4	3/16	1/8	1/16	0
	Terminal	0	0	0	0	0
		← THOMAS EFFECT				

Basal buoyancy factor $\phi_B = \phi\, \phi_O$ decreases from 1A to 5E defined as:

Increasing ice-bed coupling beneath an ice stream

ZWALLY EFFECT ↑

1. Full basal buoyancy along entire length ($\phi = 1$).
2. Basal buoyancy slowly decreasing upstream.
3. Basal buoyancy steadily decreasing upstream.
4. Basal buoyancy rapidly decreasing upstream.
5. No basal buoyancy along entire length ($\phi = 0$).

Increasing ice-shelf buttressing beyond the ice stream

THOMAS EFFECT ↑

A. No ice shelf or a freely floating ice shelf ($\phi_O = 1$).

B. Weak buttressing by a confined and pinned ice shelf.

C. Moderate buttressing by a confined and pinned ice shelf.

D. Strong buttressing by a confined and pinned ice shelf.

E. Full buttressing by a fully confined ice shelf or an ice lobe ($\phi_O = 0$).

CC BY

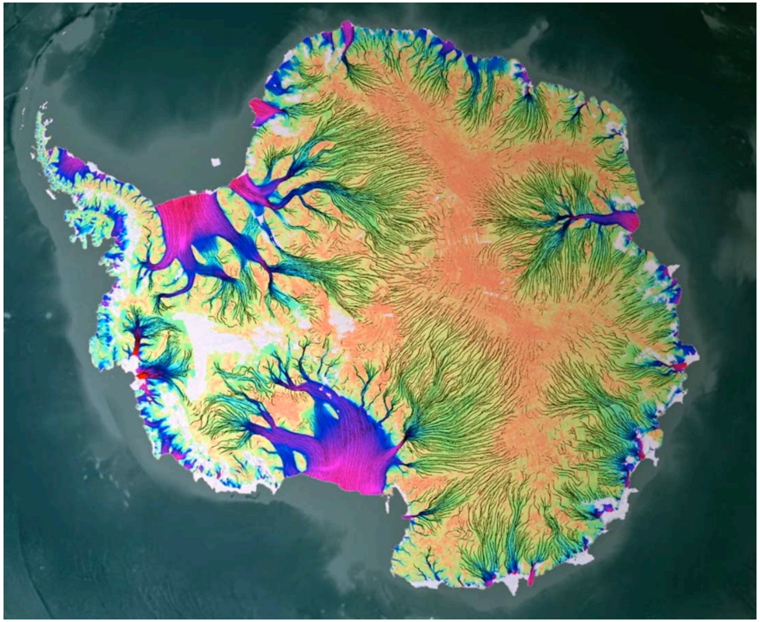

Fig. 1. A full map of Antarctic ice flow showing tributaries supplying major ice streams. This map was compiled by NASA-funded research at the Jet Propulsion Laboratory of the California Institute of Technology and the University of California at Irvine, using data from Earth-orbiting satellites provided by the Japanese, European, and Canadian Space Agencies. Ice velocities increase from orange near interior ice divides to green in ice tributaries to blue in ice streams to red on ice shelves. A video showing motion of the tributaries is available on the NASA News website. From Rignot et al. (2011).

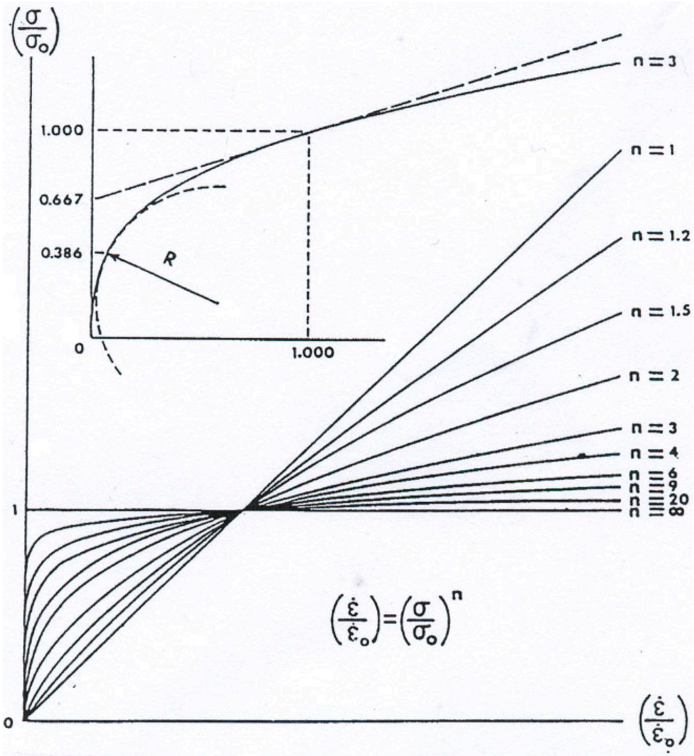

Fig. 2. The viscoplastic creep spectrum for steady-state creep in crystalline materials. Applied stress σ causes strain rate $\dot{\varepsilon}$ in the expression $\dot{\varepsilon} = \dot{\varepsilon}_O(\sigma/\sigma_O)^n$ where viscoplastic exponent n varies from unity to infinity, σ_O is the plastic yield stress, and $\dot{\varepsilon}_O$ is the strain rate at σ_O for all values of n. The inset shows two criteria to obtain a viscoplastic yield stress σ_V for ice, taking $n = 3$. The tangent to the curve at $\dot{\varepsilon}_O$ gives $\sigma_V = 0.667\sigma_O$. The maximum curvature of the curve gives $\sigma_V = 0.386\sigma_O$. From Hughes (1998, Chapter 8).

TCD
8, 2043–2118, 2014

Quantifying the Jakobshavn Effect

T. Hughes et al.

CC BY

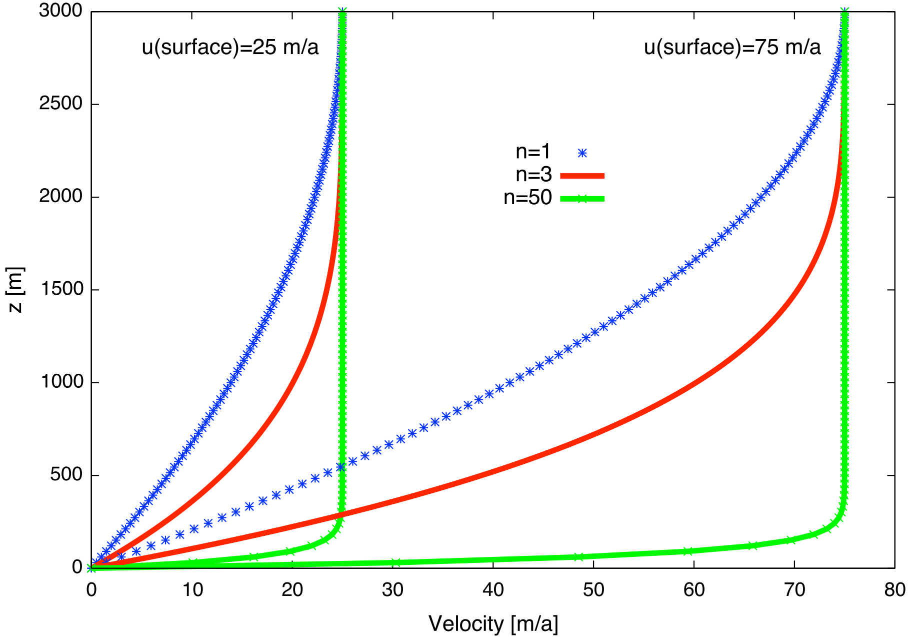

Fig. 3. Vertical profiles of horizontal ice velocity for sheet flow in ice 3 km high. Profiles are for $n = 1$ for viscous flow, $n = 3$ for ice flow, and $n = 50$ for plastic flow in Eq. (6) when the surface velocity is $75\,\mathrm{m\,a^{-1}}$ in ice tributaries and 25 m between ice tributaries in Fig. 1. Warmer ice having an easy-glide ice fabric near the bed causes n to increase if A is artificially kept constant. Velocity profiles will be between those for $n = 3$ and $n > 50$, with n in tributaries being higher than n between tributaries. In tributaries, the rapid increase in velocity just above bedrock at $z = 0$ is caused by ice sliding over deforming wet till. This uncertainty makes combining the force, mass, and energy balance problematic.

CC BY

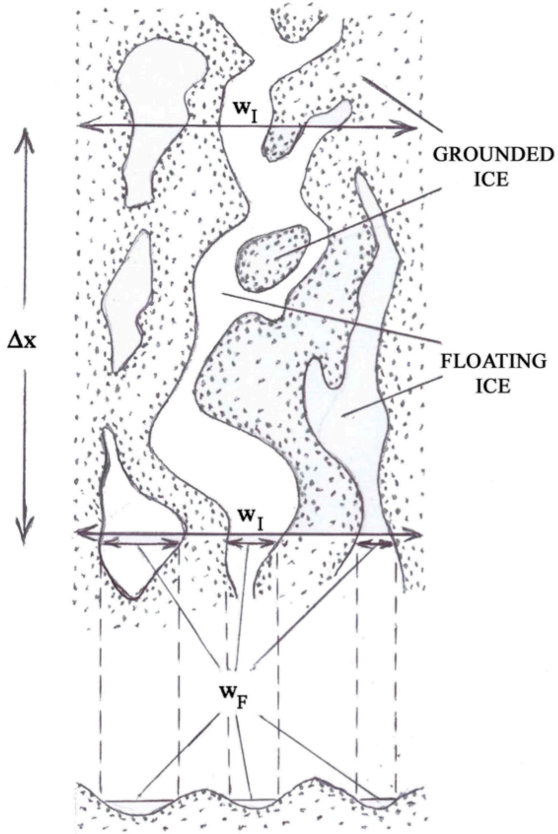

Fig. 4. A cartoon of the bed under an ice stream. Ice flow is along incremental length Δx in plan view (top) and at x in transverse cross-section (bottom). Ice is either floating above bedrock or supersaturated sediments and till (undotted areas) or grounded on bedrock or unsaturated sediments and till (dotted areas) for respective floating flowband widths w_F and grounded flowband widths $w_I - w_F$. Floating fraction φ of ice over area $w_I \Delta x$ becomes $\varphi = w_F / w_I$ at x when $\Delta x \to 0$.

TCD
8, 2043–2118, 2014

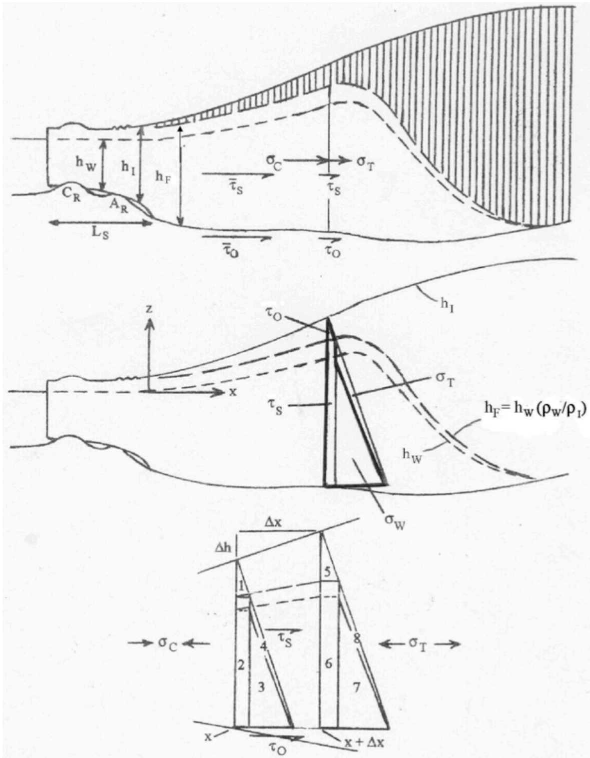

Fig. 5. The geometrical force balance on an ice stream ending as a confined ice shelf. Top: resisting stresses that resist gravitational flow. The bed supports ice in the shaded area. Ice in the unshaded area is supported by basal water pressure. Middle: gravitational forces at x represented as triangles and a rectangle are linked to specific resisting stresses. The area inside the thick border is linked to σ_C. Heights h_I, h_W, and h_F are measured from the bed for $x > 0$. Bottom: resisting stresses and gravitational forces along Δx. Resisting and gravitational forces are balanced along x and Δx.

TCD
8, 2043–2118, 2014

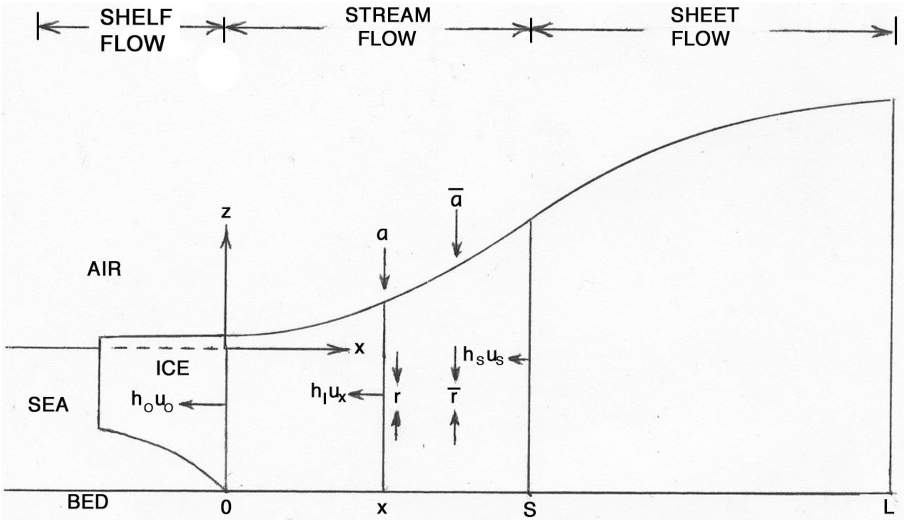

Fig. 6. A longitudinal profile of an ice-sheet flowband of constant width on a horizontal bed showing components of the mass balance for sheet, stream, and shelf flow from right to left. Ice thickness h_l and mean ice velocity u_x are shown at the ungrounding line ($x = 0$), along an ice stream (x), at the beginning of stream flow ($x = S$), and at the beginning of sheet flow ($x = L$) for mean accumulation rate $\overline{a}$ and ice thinning rate $\overline{r}$ averaged along x, and rates a and r at x. These same components exist for variable bed topography.

CC BY

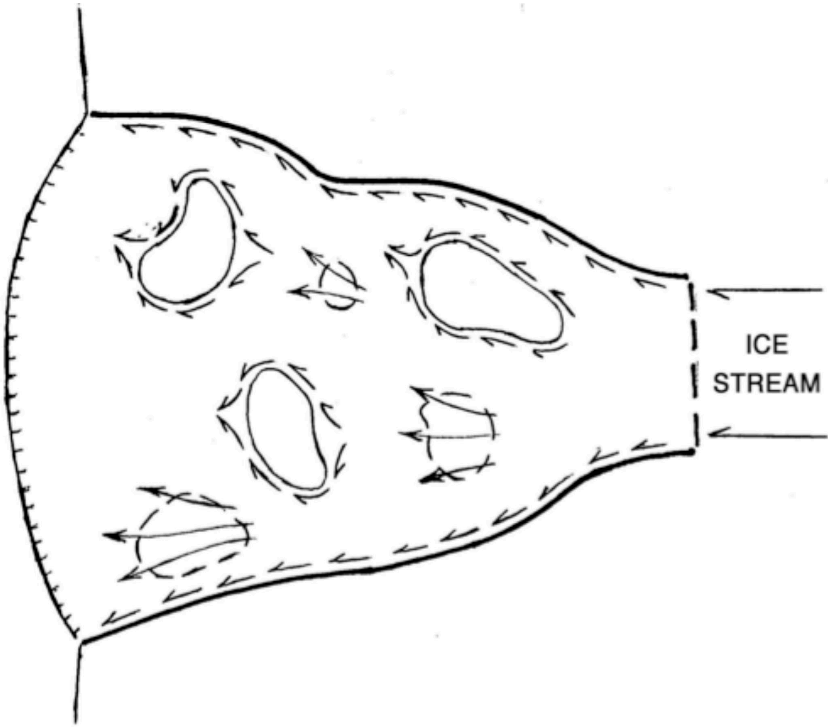

Fig. 7. A cartoon showing an ice stream entering a confined and pinned ice shelf. Shelf flow is from the ice stream grounding line (heavy dashed line) to the ice-shelf calving front (hachured line), with flow shearing along the sides of a confining embayment (half arrows alongside thick solid lines), around ice rises (half arrows alongside thin solid lines), and over ice rumples (full arrows across thin dashed lines).

TCD
8, 2043–2118, 2014

Quantifying the Jakobshavn Effect

T. Hughes et al.

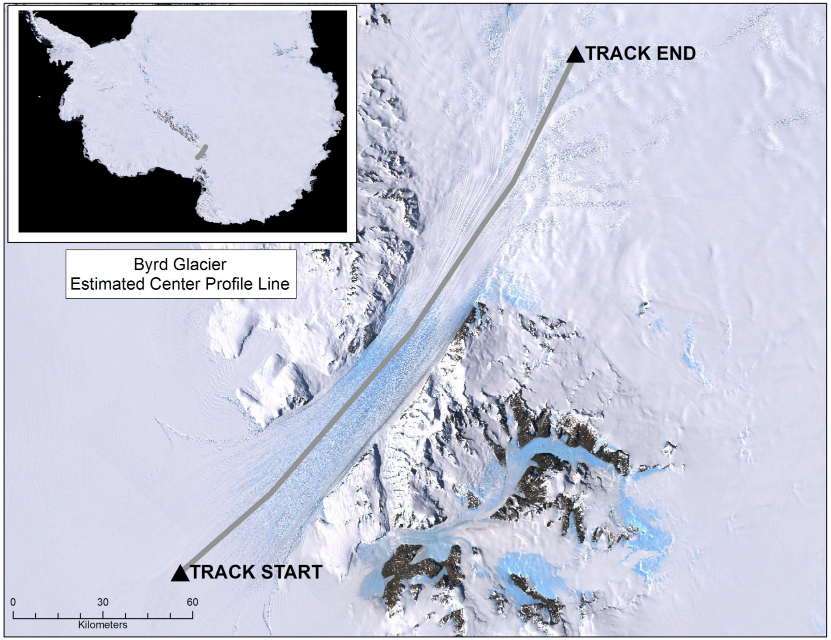

Fig. 8. A satellite image of Byrd Glacier showing the centerline along which the ice surface, base, and thickness were determined by radar sounding. The inset locates Byrd Glacier supplying the Ross Ice Shelf in Antarctica.

CC BY

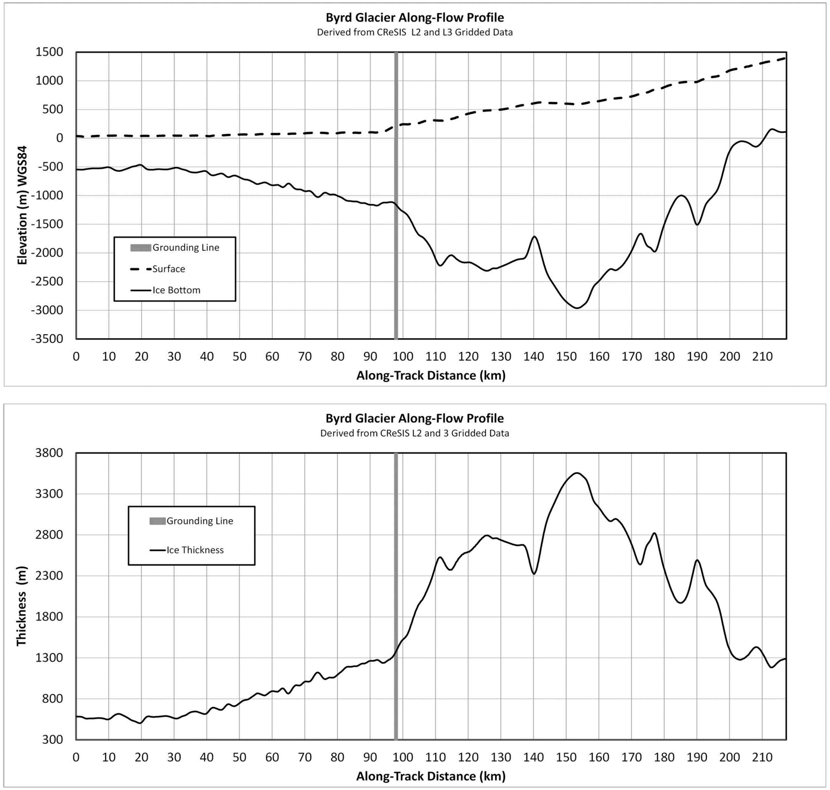

Fig. 9. Surface, base, and thickness radar profiles down the centerline of Byrd Glacier shown in Fig. 8. The vertical line separates grounded ice (left) from floating ice (right) where the flotation criterion is still approximately satisfied nearly 100 km from the track start in Fig. 8. Top: ice surface (dashed line) and ice base (solid line). Bottom: ice thickness.

CC BY

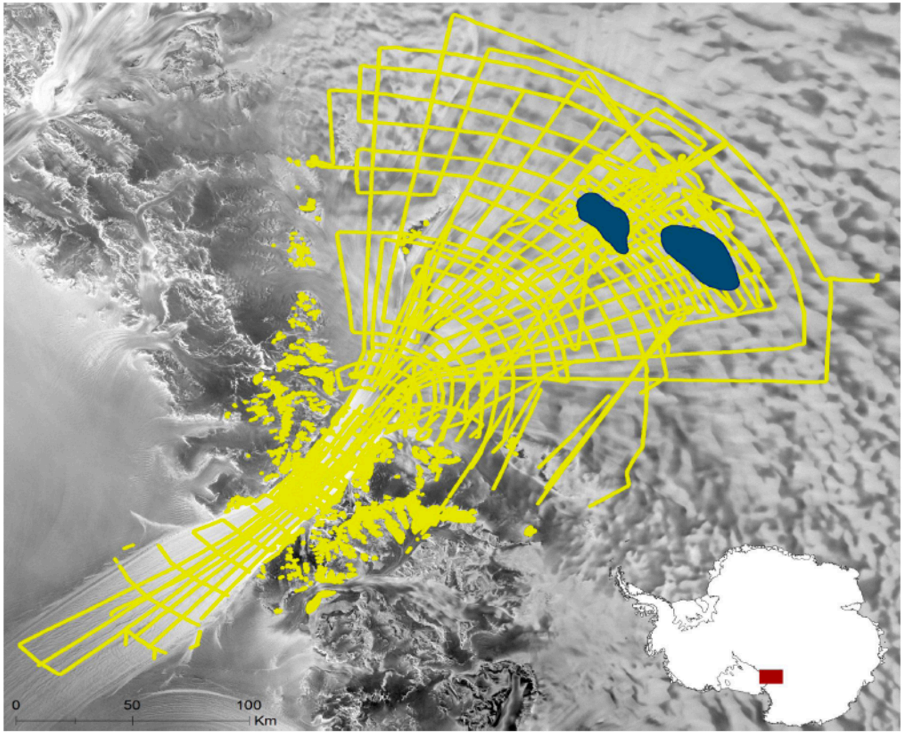

Fig. 10. A map showing Byrd Glacier in relation to the two subglacial lakes that drained suddenly in 2006–2007. The lakes are green. Radar flightlines are in yellow, with the fan of flightlines flown along ice flowlines. The inset map locates this region of Antarctica as the red rectangle. Map provided by Leigh Stearns.

CC BY

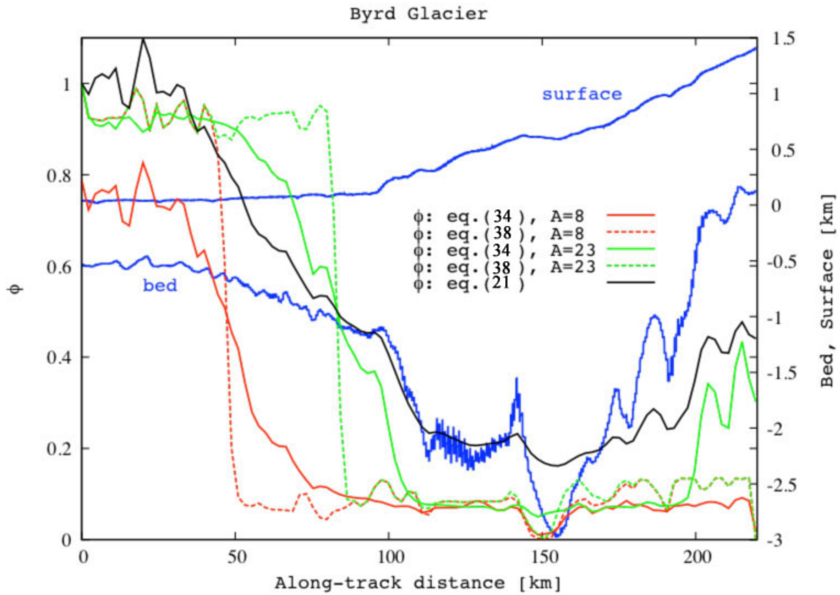

Fig. 11. Plots of floating fraction φ of ice along Byrd Glacier obtained from Eqs. (34), (38), and (21). Blue lines are the top and bottom surfaces of Byrd Glacier for both grounded and floating ice. Variations of φ along x are from Eq. (34) for a flowband the width of Byrd Glacier with side shear and from Eq. (38) for the central flowline with side shear incorporated into basal shear. The two plots cross for values of hardness parameter A that locate grounding lines at about 50 and 80 km from the beginning of the radar profile. Both locations satisfy the flotation criterion for locating the ungrounding line of Byrd Glacier. The higher value of A puts φ closer to $\varphi = 1$ required for fully floating ice. Eqs. (34) and (38) use both the force balance and the mass balance. The φ plot for Eq. (21) uses only the force balance. All φ plots are compatible with an ungrounding line 40 to 50 km from the beginning of the radar flightline in Fig. 8.

CC BY

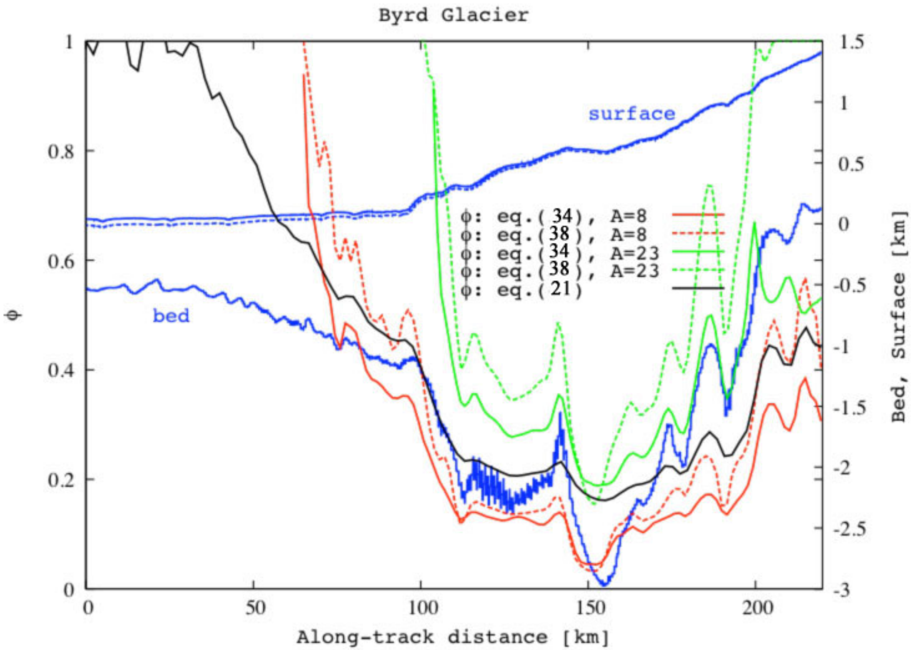

Fig. 12. Plots of floating fraction φ along Byrd Glacier if the discharge of lake water had been sustained. Equations (34), (38), and (21) are solved for φ when ice thickness is reduced linearly from zero to ten percent along Byrd Glacier to accommodate the ten percent increase in ice velocity at the ungrounding line while the two subglacial lakes in Fig. 10 were draining. This thinning did not take place in real time, but it would have if the faster ice discharge rate of ice were sustained over time, with a corresponding reduction in ice-bed coupling. Note how the choice of A affects the position of the ungrounding line. Blue lines are the top and bottom surfaces of Byrd Glacier. The "bed" includes floating basal ice. Including side shear, Eq. (34), reduces φ.

CC BY

CC BY

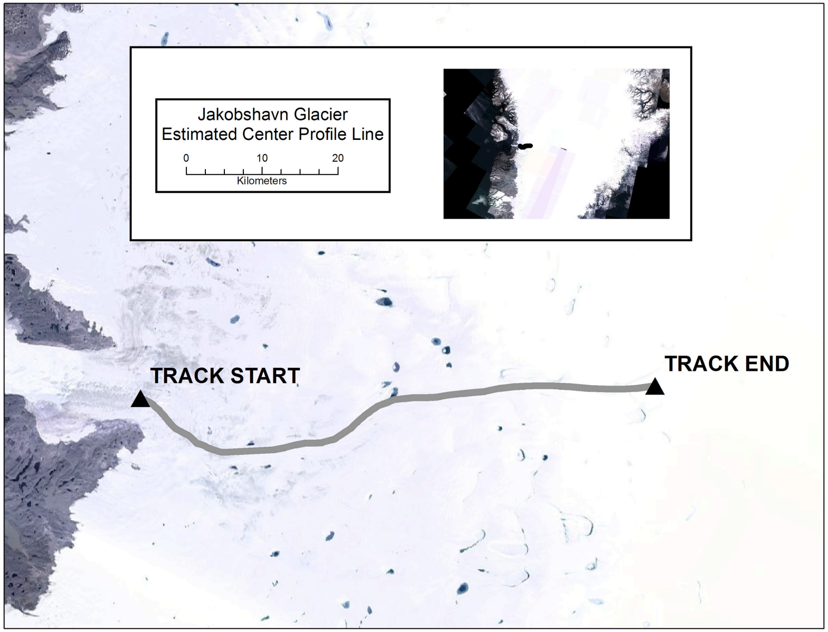

Fig. 13. A satellite image of Jakobshavn Isbrae showing the centerline along which the ice surface, base, and thickness were determined by radar sounding. The inset map locates Jakobshavn Isbrae in the Greenland Ice Sheet (black rectangle).

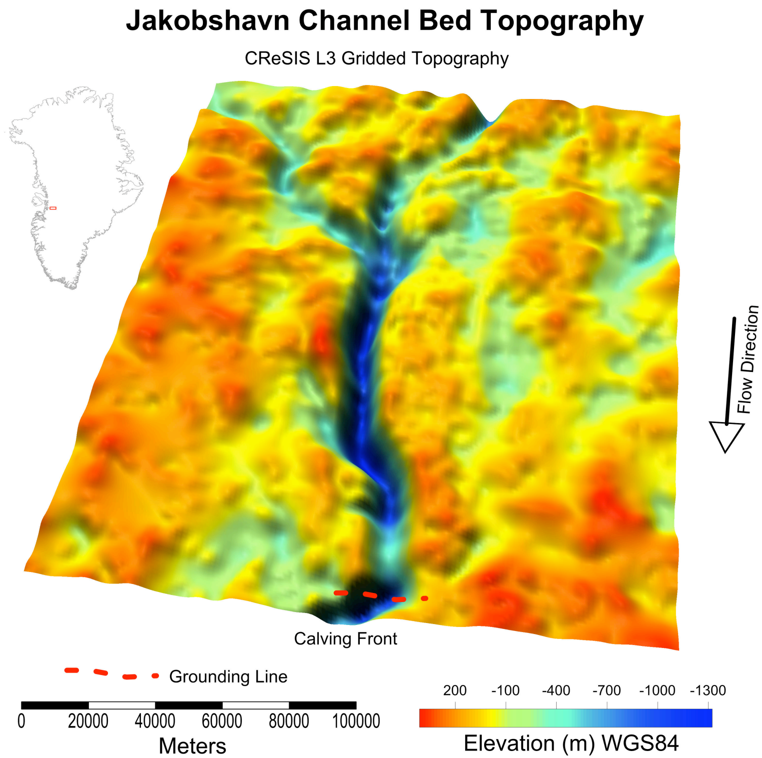

Fig. 14. "Gogineni Gorge" and surrounding bed topography beneath ice entering Jakobshavn Isbrae. The radar track in Fig. 13 is along the centerline of Gogineni Gorge. This map was produced from radar sounding by the Center for Remote Sensing of Ice Sheets (CReSIS) at the University of Kansas.

TCD
8, 2043–2118, 2014

Quantifying the Jakobshavn Effect

T. Hughes et al.

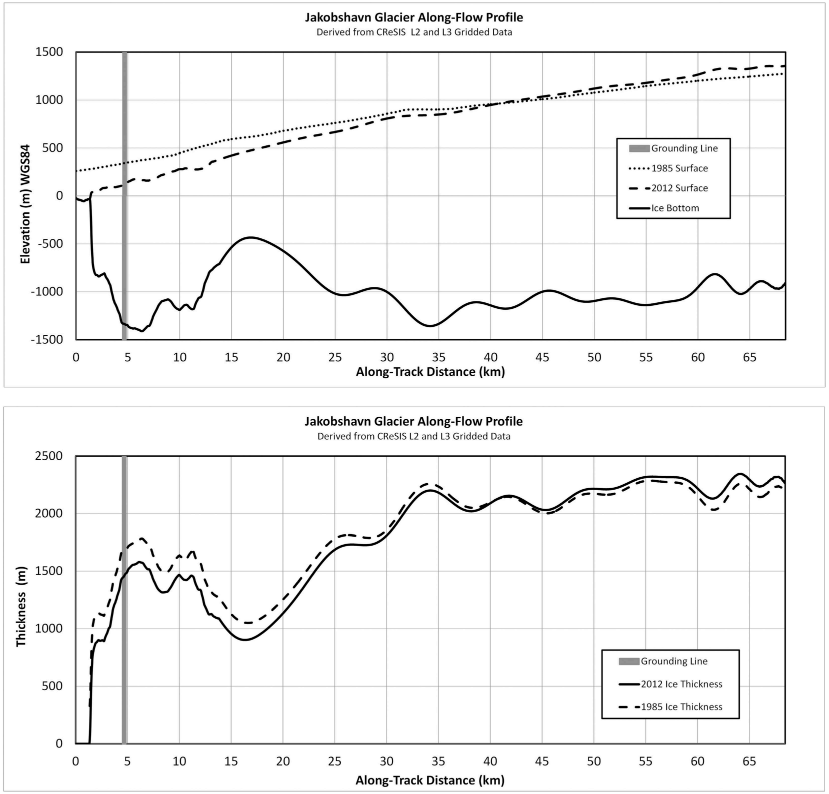

Fig. 15. Surface, base, and thickness profiles down the centerline of Jakobshavn Isbrae shown in Fig. 13. The vertical line separates grounded ice (right) from floating ice (left). Top: ice surfaces in 1985 (dotted line) and 2012 (dashed line) and ice base (solid line). Bottom: ice thickness in 1985 (dashed line) and 2012 (solid line).

cc BY

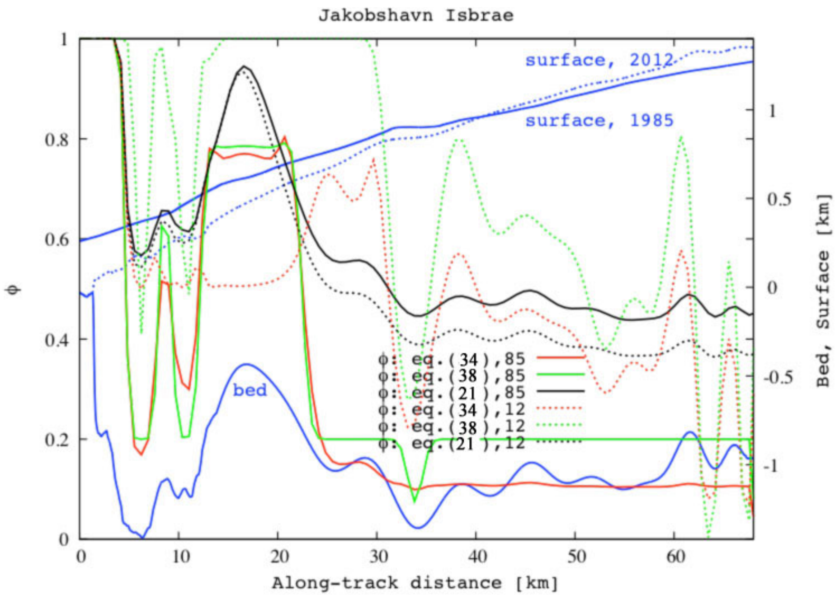

Fig. 16. Plots of floating fraction φ of ice along Jakobshavn Isbrae before and after ice-shelf disintegration. Equations (34), (38), and (21) were solved for φ using the 1985 and 2012 surface profiles. Blue lines are the top and bottom surfaces of Jakobshavn Isbrae. Variations of φ along x are from Eq. (34) for a flowband the width of Jakobshavn Isbrae with side shear and from Eq. (34) for the central flowline of Jakobshavn Isbrae with side shear incorporated into basal shear. Reasonable variations of hardness parameter A produce essentially the same variations of φ along x. The sharp drop of φ from $\varphi = 1$ for floating ice occurs where the first-order surface profile of Jakobshavn Isbrae is concave, with φ increasing from about 0.2 ± 0.1 to 0.5 ± 0.1 respectively before and after ice-shelf disintegration when the first-order surface profile is convex. Equations (34) and (38) use both the force balance and the mass balance. The φ plots for Eq. (21) uses only the force balance.

TCD
8, 2043–2118, 2014